

Is curved graphene a possible answer to the problem of graphene's diverging magnetic susceptibility?

Abdiel de Jesús Espinosa-Champo^{a,c} and Gerardo G. Naumis^b

^a Posgrado de Ciencias Físicas, Universidad Nacional Autónoma de México,
Apartado Postal 20-364 0100, Ciudad de México, México and

^b Departamento de Sistemas Complejos, Instituto de Física,
Universidad Nacional Autónoma de México, Apartado Postal 20-364 01000, Ciudad de México, México.

Pavel Castro-Villarreal^{c*}

^c Facultad de Ciencias en Física y Matemáticas, Universidad Autónoma de Chiapas,
Carretera Emiliano Zapata, Km. 8, Rancho San Francisco,
C. P. 29050, Tuxtla Gutiérrez, Chiapas, México.

A study of curved graphene in the presence and absence of a real magnetic field is conducted to determine the magnetization and magnetic susceptibility. Utilizing a Dirac model, the Landau level energy corrections are found. These results are compared with those obtained from a tight-binding model analysis, showing good agreement with the Dirac model. The obtained spectra are then used to calculate the free energy, magnetization, and magnetic susceptibility as functions of the external magnetic field and curvature. The resulting de Haas van Alphen (dHvA) effect exhibits distinctive signatures due to the curvature of graphene, including a resonance effect when the pseudomagnetic and the real magnetic fields are equal. Considering that curvature induces effective pseudomagnetic fields, a mechanical effect stemming from an electronic contribution is found, resulting in a pseudo-de Haas van Alphen (pdHvA) effect without needing an external magnetic field. This effect is associated with oscillating (electronic) forces opposing deformations. These forces, divergent in flat graphene, suggest that graphene (without a substrate) attains mechanical equilibrium through local corrugations. These mechanical deformations prevent the theoretically calculated pristine graphene's diamagnetic divergence at low temperatures, indicating that corrugations produce a finite, experimentally measurable magnetic susceptibility. The divergent susceptibility becomes apparent only when such corrugations are removed using various strategies.

I. INTRODUCTION

The de Haas van Alphen effect (dHvA) is a fascinating phenomenon that has attracted the attention of many physicists over the years [1–20]. It refers to periodic oscillations in metal magnetization when subjected to a magnetic field at low temperatures [1, 5, 9, 21–24]. These oscillations are caused by quantization of the electron energy levels in the magnetic field [8, 9, 25], and their frequency is proportional to the cross-sectional area of the Fermi surface of the sample [26].

The de Haas van Alphen effect was first discovered by Wander Johannes de Haas and Pieter M. van Alphen in 1930 while studying bismuth magnetization in a high magnetic field [1]. Later, it was realized that the effect is a general phenomenon that occurs in any metal or semiconductor with a Fermi surface [6, 8, 15, 17]. In two-dimensional electron gases (2DEGs), the dHvA effect is fascinating because the quantization of electron energy levels is more pronounced as a result of the dimensionality reduction of the system [9, 13, 18, 27]. This makes the effect a powerful tool for studying the electronic properties of quasi- and two-dimensional materials [6, 10, 11, 14, 21, 28]. This effect has also been extensively studied in 2DEGs formed at the interface between

two semiconductors [4, 5, 29, 30].

One of the most exciting aspects of the de Haas van Alphen effect in 2DEGs is the observation of sawtooth oscillations [13, 27], which are caused by the fractional filling of the Landau levels (LLs) under a magnetic field. These oscillations provide a powerful tool for studying the fractional quantum Hall effect [31], which is a striking manifestation of strong electron-electron interactions in 2DEGs.

A natural setting to study the dHvA effect is on two-dimensional materials beyond the 2DEGs. In recent years, there has been a growing interest in exploring this effect in two-dimensional materials beyond 2DEGs. For example, this effect has been experimentally observed in graphene [14, 24].

Graphene is a two-dimensional material comprising a single layer of carbon atoms arranged in a honeycomb lattice with remarkable properties [32, 33]. For example, when graphene is deformed, the Dirac points are separated, and the Fermi surface becomes a series of deformed circles [34–36]. These deformations in graphene produce a pseudomagnetic field [36–46], which can lead to pseudo-Landau levels (P-LL) [37–39, 43, 47–57]. Also induce corrections to the Quantum Hall effect (QHE) [47], pseudomagnetic QHE [58], anomalous dHvA effect in strained graphene [2, 12], Klein tunneling on negatively curved graphene sheets [59], flat bands [60–67] and many other geometrical effects on the electronic properties [36, 41, 42, 68–70], which allow posing the concept of *curvatronics*, that is, consider the curvature as a tun-

* e-mail: pcastrov@unach.mx ; author to whom correspondence should be addressed.

able parameter to control the electronic properties of the material [71]. Specifically, this enables curved graphene to have several potential applications. One possible application is in the field of valleytronics, which aims to use the valley degree of freedom of electrons in graphene rather than their charge to transmit and process information, and the curvature could be used to polarize the valley of electrons, allowing the creation of new types of valleytronic devices [2, 68, 72]. Understanding the magnetic, electronic, and thermodynamic properties of curved graphene is crucial for a comprehensive understanding of this material's behavior.

Because curvature induces effects similar to those found for magnetic fields, we present a study of curved graphene under magnetic fields in this work. In particular, we will show that curvature induces discrete spectra of the allowed energies (LLs) and a discontinuity in the magnetization with periodicity $1/B$ leading to an effective dHvA effect. For free-standing graphene, this allows us to propose a potential curvature-induced mechanism to address the issue of the theoretically calculated divergence of magnetic susceptibility at low temperatures. It is important to note that the suggested mechanism is rooted in corrugations. This does not preclude the experimental observation of such divergence, as curvature can permanently be eliminated through strain or encapsulation using other materials [73].

We have organized this paper as follows. In Sec. II, we present the simplest model to describe curved graphene under magnetic fields, both in its continuum model using the Dirac equation formalism and in the tight-binding model. In Sec. III, we calculate the LLs for two curvature regimes using the continuum model and show their effects on the Local Density of States (LDOS) obtained with the tight-binding model. In Sec. IV, we briefly review the dHvA effect in flat graphene with a constant charge carrier density and near-zero temperature. This review establishes the techniques to be used in the following sections. In Sec. V, we study the dHvA effect in strongly curved graphene and under a real magnetic field. In Sec. VII, we briefly discuss the physical differences between magnetization and pseudo-magnetization. In Sec. VI, we present the mechanical effect produced by the electronic contribution in graphene and how this gives rise to a pseudo-de Haas van Alphen effect (pdHvA) due only to curvature. Finally, in Section VIII, we present our conclusions and future perspectives.

II. GRAPHENE ELECTRONIC MODELS

This section presents the details of the models we will consider and how they relate. This section is divided into two parts. In the first, we provide the Dirac Hamiltonian for curved graphene, and in the second, we study the same system from the perspective of a tight-binding Hamiltonian. It is worthwhile to mention that such a system can also be studied by using perturbation theory [50, 52]. However, the curved-space method offers sev-

eral distinctive advantages. Specifically, this approach allows for the natural handling of non-planar geometries and local deformations, such as bumps, which are common in corrugated graphene structures. In comparison to perturbation theory, often used to address slightly perturbed systems around a known base state, the curved-space method provides a description where the effects of curvature dominate the behavior of electrons in graphene. While perturbation theory has proven effective in specific contexts [50, 52], the curved-space method has the potential to offer a unique perspective, allowing to analytically study more complex phenomena such as dislocations [59]. Furthermore, it may facilitate establishing analogies with systems from other fields of physics in a natural manner [46, 74, 75].

A. Dirac model for curved graphene in an external magnetic field

This section introduces the simplest model to describe the electronic degrees of freedom of a curved graphene sheet under a uniform magnetic field. In Fig. 1, we present two limiting examples of such deformations. To introduce a model for describing such systems, we begin with the Dirac equation in the presence of electromagnetic fields for massless Dirac fermions [40, 47, 76–86]

$$i\hbar\gamma^{\alpha}\left(\nabla_{\alpha}-i\frac{q}{\hbar}A_{\alpha}\right)\psi=0, \quad (1)$$

where q is the charge's particle, and the electromagnetic vector potential, denoted as A_{α} , is defined on a $2+1$ dimensional curved space-time \mathbb{M} . The Dirac matrices $\gamma^{\mathcal{A}}$ satisfy the Clifford algebra $\{\gamma^{\mathcal{A}},\gamma^{\mathcal{B}}\}=2\eta^{\mathcal{A}\mathcal{B}}\mathbb{1}_{2\times 2}$, with $\eta_{\mathcal{A}\mathcal{B}}$ the Minkowski metric tensor and $\underline{\gamma}^{\alpha}(x)=\gamma^{\mathcal{A}}e_{\mathcal{A}}^{\alpha}(x)$. The set $\{e_{\mathcal{A}}^{\alpha}(x)\}$ consists of dreibeins associated with each coordinate patch of \mathbb{M} . Here, the capital and italic Latin indices \mathcal{A} represent the Minkowski flat coordinates, while the Greek indices α indicate the local curved coordinates.

The covariant derivative for the spinor representation of the Lorentz group $SO(2,1)$ is given by $\nabla_{\alpha}=\partial_{\alpha}+\Omega_{\alpha}$, where $\Omega_{\alpha}=\frac{1}{4}\omega_{\alpha}^{\mathcal{A}\mathcal{B}}s_{\mathcal{A}\mathcal{B}}$ serves as the spin connection. The components $\omega_{\mathcal{A}\mathcal{B}}^{\alpha}$ form elements of the 1-form satisfying the Maurer-Cartan equations [87]. Meanwhile, $s_{\mathcal{A}\mathcal{B}}=\frac{1}{2}[\gamma_{\mathcal{A}},\gamma_{\mathcal{B}}]$ represents the pseudo-spin operator. Thus, both $\omega_{\alpha}^{\mathcal{A}\mathcal{B}}$ and $e_{\mathcal{A}}^{\alpha}(x)$ carry the geometric essence of the Dirac equation. The metric tensor of the space-time \mathbb{M} can be expressed using dreibeins, denoted by $g_{\alpha\beta}=e_{\alpha}^{\mathcal{A}}(x)e_{\beta}^{\mathcal{B}}(x)\eta_{\mathcal{A}\mathcal{B}}$.

Here, we consider a stationary spacetime with global structure $\mathbb{M}=\mathbb{R}\times\Sigma$, whose spatial sector Σ is a two-dimensional curved surface, *i.e.* with a metric given by $ds^2=-v_F^2dt^2+g_{ij}dx^i dx^j$, being g_{ij} the metric tensor of Σ with $i,j=1,2$, and v_F is the Fermi velocity. In addition, we consider that the electromagnetic potential A_{α} has only spatial components, that is, $A_0=0$. In the following, we proceed to separate the indices \mathcal{A} and α into time and spatial components, $\{0,a\}$ and $\{0,j\}$, respectively. Thus, the dreibeins for this metric are $e_0^0=$

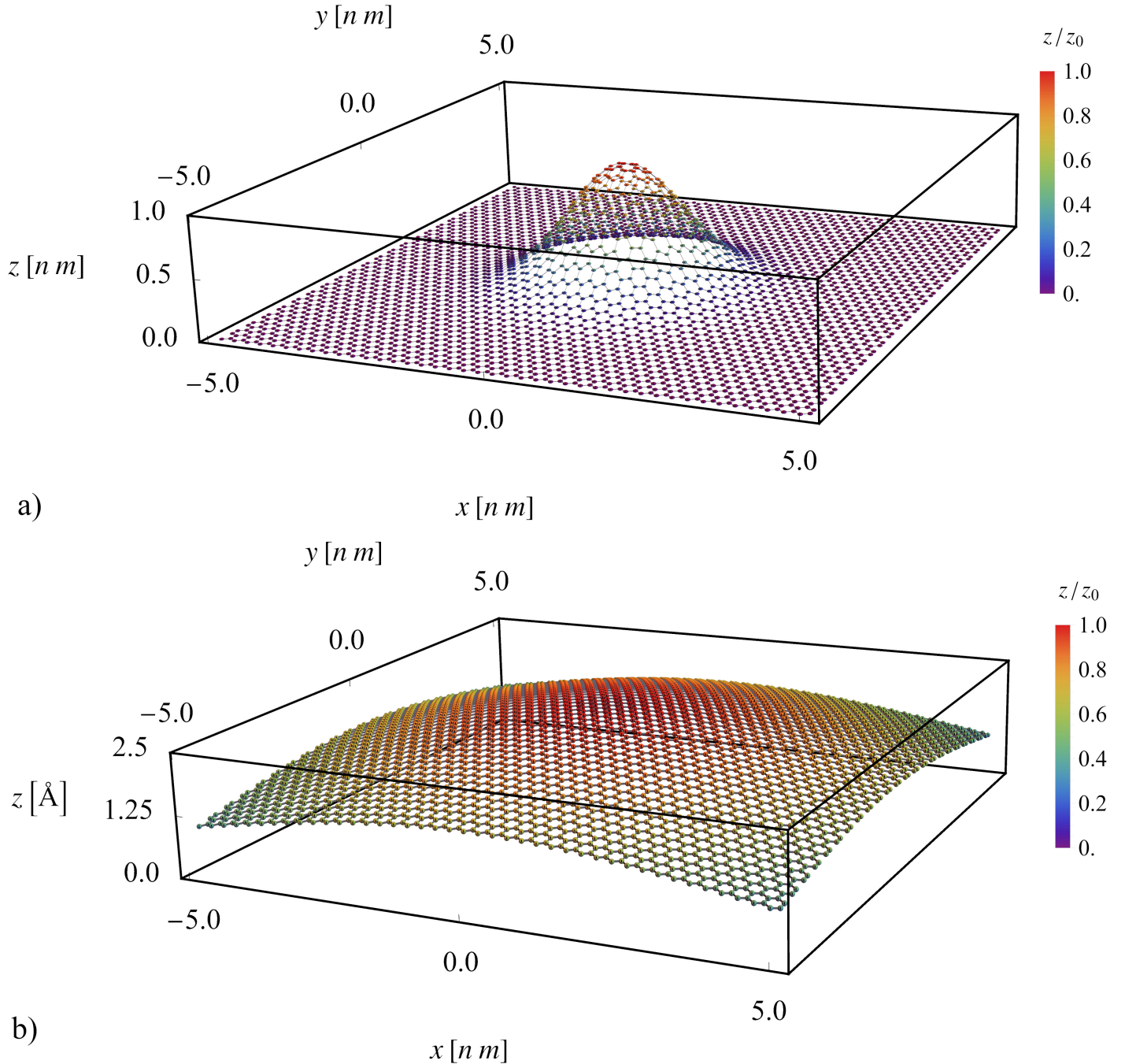


FIG. 1. Graphene sheet with dimensions $L_x = L_y = 10$ nm deformed in such a way as to generate a Gaussian bump whose profile is given by Eq. (A11). As mentioned in Appendix A, the parameter that controls the type of regime established is the ratio between the height of the bump z_0 and the standard deviation ϖ^2 , that is, $(z_0/\varpi^2)^2 = R(r=0 \text{ nm})$. a) For this case, we set $z_0 = 1$ nm and $\varpi = 1$ nm such that $(z_0/\varpi^2)^2 = 1 \text{ nm}^{-2}$ establishes a strong curvature regime, while for b) we set $z_0 = 0.25$ nm and $\varpi = 5$ nm such that $(z_0/\varpi^2)^2 = 1 \times 10^{-4} \text{ nm}^{-2}$ establishes a weak curvature regime. The color scale indicates the vertical position z of each site in relation to the maximum height z_0 .

1, $e_0^i = e_a^0 = 0$; and $e_a^i \neq 0$ such that $g_{ij} = e_i^a e_j^b \delta_{ab}$. Also, it can be shown that $\omega_{jb}^0 = \omega_{0b}^a = \omega_{j0}^a = 0$ and $\omega_{jb}^a \neq 0$, with spatial indices a, b, i, j and k . This implies that the covariant derivative is reduced to $\nabla_0 = \partial_0$ and $\nabla_j = \partial_j + \frac{1}{4}\omega_j^{ab} s_{ab}$. This implementation of index decomposition on the Dirac equation (1) results in a Schrödinger-like

equation $i\hbar\partial_0\psi = \mathcal{H}\psi$, where $\mathcal{H} = -i\hbar v_F \gamma_0 \underline{\gamma}^j(x) \nabla_j$ with $\nabla_j \equiv \nabla_j - i\frac{q}{\hbar} A_j$. This decomposition has been studied in previous works [40, 47, 79, 88]. Additionally, the effective tensorial and space-dependent Fermi velocity $v_a^{\text{eff},j}(x) = v_F e_a^j(x)$ can be obtained using $\underline{\gamma}^j(x) = \gamma^a e_a^j(x)$ [39, 40]. We now have all the components to write a field-theoretic

Hamiltonian for the curved sheet of graphene as

$$\hat{H} = \sum_{\xi=\pm} \sum_{\sigma=\uparrow,\downarrow} \int d^2x \sqrt{g} \psi_{\sigma,\xi}^\dagger \mathcal{H}_\xi \psi_{\sigma,\xi}, \quad (2)$$

where σ and ξ label the spin and valley indexes. The operators \mathcal{H}_+ and \mathcal{H}_- represents two Dirac operators corresponding to each valley K and K' , respectively. The difference between these operators resides in the Dirac matrix representations in each valley. We choose the particular representations of the Dirac matrices $\gamma_\xi^0 = \gamma^0 = -i\sigma_3$, $\gamma_\xi^1 \gamma_\xi^0 = \sigma^1$, and $\gamma_\xi^2 \gamma_\xi^0 = \xi \sigma^2$ with σ_3 and σ^a , $a = 1, 2$, being the standard Pauli matrices; this implies, particularly, that in the K' valley pseudo-spin operator has opposite sign with respect to K valley. For compact notation, we introduce the Dirac operators in each valley explicitly using the valley index ξ

$$\mathcal{H}_\xi = -i\hbar v_F \gamma_0 \underline{\gamma}_\xi^j(x) \nabla_j^\xi, \quad \text{with} \quad \nabla_j^\xi \equiv \nabla_j - i \frac{q}{\hbar} A_j. \quad (3)$$

In this representation, for flat graphene, it is easy to show that $\mathcal{H}_+ = -i\hbar v_F \sigma_a (\partial_a - i \frac{q}{\hbar} A_a)$, which is the low energy limit of the Wallace tight-binding model [33, 38] in the presence of electromagnetic fields once the movement of the Dirac cone tip is taken into account [34–36, 48]. This Hamiltonian \hat{H} is also similar to the cosmological model proposed by Vozmediano *et al.* [37].

We remark that the curved sheet of graphene is considered here also under a real, external magnetic induction field \mathbf{B} , which is defined in the Euclidean space \mathbb{R}^3 . The field \mathbf{B} can be expressed in terms of the $U(1)$ gauge field \mathbf{A} as usual $\mathbf{B} = \text{rot} \mathbf{A}$, where rot is the rotational operator on vector fields in \mathbb{R}^3 . It is clear that the field \mathbf{B} determines the vector field A_j on the curved surface Σ . For this purpose, it is imperative to introduce a few extrinsic elements of the curved sheet of graphene geometry. So, let us call $\mathbf{X} : \mathbb{D} \subset \mathbb{R}^2 \rightarrow \Sigma \subset \mathbb{R}^3$ a parameterization of the surface, where \mathbb{D} is a domain and $\mathbf{X}(x^i)$ is vector position in \mathbb{R}^3 on a certain point p of the surface Σ . Since the charge carriers move intrinsically on the surface, their electromagnetic moment $\frac{q}{\hbar} A_j$ must be tangent to the surface, therefore the magnetic potential can be written as $A_j(x^i) = \mathbf{e}_j(x^i) \cdot \mathbf{A}(\mathbf{X}(x^i))$, where $\mathbf{A}(\mathbf{X})$ is the $U(1)$ gauge field at the point p on the surface, and $\{\mathbf{e}_j(x^i) = \partial_j \mathbf{X}(x^i)\}$ is a set of tangent vectors at p .

We add that due to the introduction of a complex phase in Eq. (1), the application of a real magnetic field in graphene breaks the time-reversal symmetry. The pseudomagnetic field that arises from the graphene's curvature is different in the sense that it does not break such symmetry [36]. This can be seen from Eq. (2) as the graphene valleys K and K' are related by time-reversal symmetry once the real magnetic field is removed. This matter will be studied in more detail in the context of the resulting spectrum.

B. Tight-binding (TB) model for a curved graphene in a magnetic field

To better understand and compare some of the results from the previously discussed effective model, we also explore a numerical implementation of a tight-binding (TB) model for curved graphene under a real, external magnetic field.

The TB Hamiltonian of the model is defined as follows,

$$\mathcal{H} = \sum_{\langle nm \rangle} t_{nm}(\mathbf{r}) \hat{c}_{\mathbf{r}_n}^\dagger \hat{c}_{\mathbf{r}_m} + h.c. \quad (4)$$

Here, $\langle nm \rangle$ represents the sum over the neighbors with positions \mathbf{r}_n and \mathbf{r}_m that satisfy $|\mathbf{r}_n - \mathbf{r}_m|^2 - (\mathbf{r}_n - \mathbf{r}_m)_z^2 \leq a_c^2$ with $a_c = 1.42 \text{ \AA}$ the interatomic distance in flat graphene; $\hat{c}_{\mathbf{r}_n}^\dagger$ ($\hat{c}_{\mathbf{r}_n}$) is the creation (annihilation) operator and $t_{nm}(\mathbf{r})$ is the hopping integral between the n -th and m -th sites, given by

$$t_{nm}(\mathbf{r}) = t_0 e^{i \frac{2\pi}{\Phi_0} \int_{\mathbf{r}_n}^{\mathbf{r}_m} \mathbf{A}_{nm} \cdot d\mathbf{l}} e^{-\bar{\beta}(|\mathbf{r}_n - \mathbf{r}_m|^2 - a_c^2)/a_c}, \quad (5)$$

where $t_0 = -2.8 \text{ eV}$. \mathbf{A}_{nm} is the vectorial potential along the path that joins sites n and m , $\Phi_0 = h/e$ is the magnetic flux quantum, $\bar{\beta} = 3.37$ is the Grüneisen parameter [36, 72]. The Fermi velocity in flat graphene can be computed as $v_F = \frac{3t_0 a_c}{2\hbar} \approx 9.06104 \times 10^5 \text{ m/s}$. In the present study, the eigenvalues and eigenfunctions resulting from the TB model Hamiltonian, given by Eq. (4), were obtained using the Pybinding package [89].

Note that, as a consequence of curvature, the p_z orbitals become misaligned [51]. To account for this effect, it is necessary to introduce an additional correction term to the hopping parameters [62], such that the new hopping parameters are given by

$$\tilde{t}_{nm}(\mathbf{r}) = [1 + \kappa(1 - \hat{\mathbf{N}}_n \cdot \hat{\mathbf{N}}_m)] t_{nm}(\mathbf{r}) \quad (6)$$

where $\kappa \approx 0.4$, $\hat{\mathbf{N}}_i$ is the unit normal vector to the curved graphene, given by

$$\hat{\mathbf{N}}_i = \frac{\hat{e}_z - \nabla z_i}{\sqrt{1 + |\nabla z_i|^2}}, \quad (7)$$

with z_i representing the height of the i -th site, $\nabla = (\partial_x, \partial_y)$ is the two-dimensional gradient operator, and \hat{e}_z is the unit vector perpendicular to the flat graphene. Here, the term $\kappa(1 - \hat{\mathbf{N}}_i \cdot \hat{\mathbf{N}}_j)$ accounts for the change in relative orientation between the π orbitals [62]. The numerically obtained maximum value of this term in the strongly curved systems considered in this work is approximately,

$$\kappa(1 - \hat{\mathbf{N}}_i \cdot \hat{\mathbf{N}}_j) \approx 3.9 \times 10^{-3} \ll 1. \quad (8)$$

In fact, Eq. (5) can be used for systems with curvature $R \leq 1 \text{ nm}^{-2}$ and involving more atoms to optimize numerical calculations. From these previous considerations, we will neglect π orbital misalignment effects in what follows.

III. SPECTRA IN FLAT AND CURVED GRAPHENE AND DENSITY OF STATES (DOS)

This section is divided into two subsections. In the first subsection, we calculate the LLs for flat graphene under a real external magnetic field, while in the second one, we obtain the LLs for curved graphene under such an external magnetic field.

A. Landau Levels in flat graphene under a magnetic field revisited.

We first consider the Dirac equation for a 2+1 Minkowskian spacetime in a transverse induction magnetic field, $\mathbf{B} = (0, 0, B)$, and $\mathbf{A} = (0, Bx, 0)$ its corresponding vector potential in the Landau gauge. The one-particle Hamiltonian is then given by [3, 7, 22, 72]

$$\mathcal{H} = v_F \hat{\sigma} \cdot \hat{\pi}, \quad (9)$$

in which $\hat{\sigma} = (\xi\sigma_1, \sigma_2)$, where σ_j is the j -th Pauli matrix, $\xi = +1(-1)$ for the K (K') valley, and $\hat{\pi}$ is the canonical momentum with the Peierls substitution ($\hat{\pi} = \hat{p} + e\mathbf{A}$). From the Schrödinger-Dirac time-independent equation $\mathcal{H}\Psi = \varepsilon\Psi$, we obtain the known energy spectra [3, 90]

$$\varepsilon_n = \text{sign}(n)v_F\sqrt{2|n|\hbar eB}, \quad n \in \mathbb{Z}, \quad (10)$$

and which does not depend on the valley index, so there is a valley degeneration. These energies (10) are related to the emergence of LLs. In addition, in Fig. 2 it is shown the Local Density of States (LDOS) for a finite sample of graphene with area 10^2 nm^2 , which was numerically calculated via diagonalization of the Hamiltonian Eq. (4). In particular, in this figure, we compare the smallest energy eigenvalues from Eq. (10) with the results obtained from the numerical results of LDOS.

B. Landau Levels in curved graphene under a real magnetic field.

This section is devoted to adapting the methods used in the previous section to find the spectrum of curved graphene under a magnetic field. Here, we shall use a local frame defined by the so-called Riemann normal coordinates (RNCs) $y = x - x'$, where x' is a fiducial point that can be chosen as the origin [91]. We carry out the transformation $\tilde{\psi}_{\sigma,\xi} = g^{\frac{1}{4}}\psi_{\sigma,\xi}$ in the Hamiltonian (2) to capture the geometrical data coming from the area element, thus, (2) can be cast in the form

$$\hat{H} = \sum_{\xi=\pm} \sum_{\sigma=\uparrow,\downarrow} \int d^2y \tilde{\psi}_{\sigma,\xi}^\dagger \tilde{\mathcal{H}}_\xi \tilde{\psi}_{\sigma,\xi}, \quad (11)$$

where $\tilde{\mathcal{H}}_\xi = g^{\frac{1}{4}}\mathcal{H}_\xi g^{-\frac{1}{4}}$.

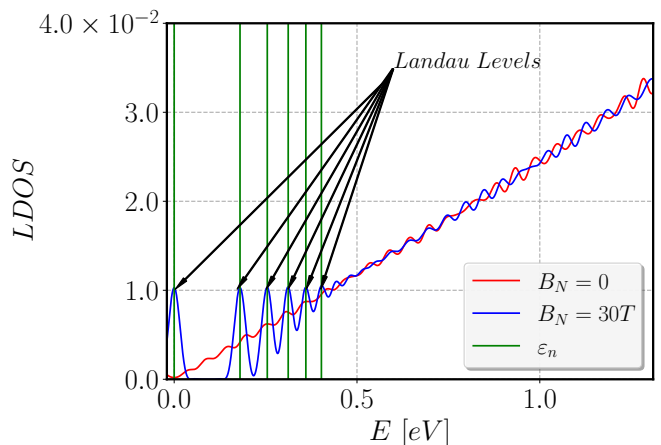


FIG. 2. Numerical calculation of the Local Density of States (LDOS) obtained from the tight-binding Hamiltonian Eq. (4) for a flat graphene sheet with dimensions $L_x = L_y = 70 \text{ nm}$ without a magnetic field (red lines) and with a magnetic field $B_z = 30 \text{ T}$ (blue lines) perpendicular to the xy plane. The field strength has been exaggerated for pedagogical reasons and to visualize the LLs (green lines) obtained from the Dirac model Eq. (10). It should be noted that for $E > 0.5 \text{ eV}$, the cases for flat graphene with and without a magnetic field are very similar. This is due to the limitation of the Dirac approximation, where $2\hbar\omega_c \sim 0.4 \text{ eV}$. In other words, as the magnetic fields become stronger, the continuum model becomes more effective at capturing information at higher energies compared to the flat graphene without magnetic fields. Furthermore, the oscillations observed in the case without a magnetic field are due to the finite size effects of the sample. As the LDOS is symmetric with respect to the zero energy, the plot is exclusively presented for $E > 0$.

Now, let be $\tilde{\mathcal{H}}_F = \tilde{\mathcal{H}}_\xi/\hbar v_F$. Further simplification can be achieved by taking the square of $\tilde{\mathcal{H}}_F$, that is, $\tilde{\mathcal{H}}_F^2 = g^{\frac{1}{4}}\mathcal{H}_F^2 g^{-\frac{1}{4}}$, where now using the Clifford algebra implies $\mathcal{H}_F^2 = -\gamma_0 \mathcal{D}_\xi \gamma_0 \mathcal{D}_\xi = -\mathcal{D}_\xi^2$, and using the Schrödinger-Lichnerowicz formula for \mathcal{D}_ξ^2 (see Appendix B) we obtain

$$\tilde{\mathcal{H}}_F^2 = -g^{\frac{1}{4}}\nabla_i^\xi g^{ij}\nabla_j^\xi g^{-\frac{1}{4}} + \frac{1}{4}R - \frac{\xi q}{2\hbar}\sigma_3\epsilon_{ij}F^{ij}, \quad (12)$$

where R is the Ricci scalar curvature, ϵ_{ij} is the 2nd order Levi-Civita tensor and $F_{ab} = \nabla_a A_b - \nabla_b A_a$ is the covariant magnetic strength tensor. This tensor is related to the external magnetic induction field \mathbf{B} applied to the curved graphene sheet. The expression of $\tilde{\mathcal{H}}_F^2$ has the same structure obtained in the context of quantum field theory in curved space [92]. The first term of (12) can be simplified in such a manner that [40]

$$\begin{aligned} \tilde{\mathcal{H}}_F^2 &= -\nabla_i^\xi g^{ij}\nabla_j^\xi - g^{-\frac{1}{4}}\partial_i \left(g^{\frac{1}{2}}g^{ij}\partial_j(g^{-\frac{1}{4}}) \right) + \frac{1}{4}R \\ &\quad - \frac{q\xi}{2\hbar}\sigma_3\epsilon_{ij}F^{ij}. \end{aligned} \quad (13)$$

This operator is the starting point to analyze the weak and strong curvature approximations, depicted in Fig. 1.

We will consider a slight curvature perturbation from the flat Hamiltonian in the weak approximation. In contrast, for the strong curvature limit, the pseudo-magnetic field associated with the curvature will be comparable to the magnetic field's value.

Next, for the aforementioned approximations, we use the fact that the metric tensor and spin connection (using RNCs) can be written as a Taylor series with coefficients given in terms of the covariant derivative of the Riemann tensor [92, 93]. The first terms of these series expansions are

$$\begin{aligned} g^{ij} &= \delta^{ij} - \frac{1}{3} R^i{}_{kl}{}^j y^k y^l + \dots, \\ \Omega_j^\xi &= \frac{\xi}{4} y^k R_{kj}{}^{ab} s_{ab} + \dots, \end{aligned} \quad (14)$$

where the dots indicate higher order terms $\mathcal{O}(y^n)$ with $n \geq 3$, and the coefficients R_{ijkl} are the components of the Riemann curvature tensor evaluated at the fiducial point x' . Here s_{ab} is the pseudo-spin operator in K valley.

Additionally, we approximate the magnetic potential A_j . According to the previous section, the gauge field can be written as $A_j = \mathbf{e}_j \cdot \mathbf{A}$. Now, for a uniform magnetic induction field \mathbf{B} let us choose the symmetric gauge thus the $U(1)$ vector potential \mathbf{A} is given by $\mathbf{A} = \frac{1}{2} \mathbf{X} \times \mathbf{B}$, where recall that \mathbf{X} are the embedding functions of the curved surface Σ . Although the magnetic field \mathbf{B} is uniform, the magnetic potential A_a may have a nonlinear dependence on the local coordinates of the surface. Expressing the embedding functions $\mathbf{X}(y)$ in terms of the RNC is not difficult to show that $\mathbf{X}(y) \approx \mathbf{e}_b y^b + \mathcal{O}(y^2)$, thus $A_a = \frac{1}{2} (\mathbf{e}_a \times \mathbf{e}_b) \cdot \mathbf{B}$. After using identity $\mathbf{e}_a \times \mathbf{e}_b = \sqrt{g} \epsilon_{ab} \mathbf{N}$ and $\sqrt{g} = 1$ at the fiducial point, we can find the first approximation of the curved magnetic potential $A_a = \frac{1}{2} B_N \epsilon_{ab} y^b + \mathcal{O}(y^2)$, where it can be shown that quadratic terms involve tangent components of \mathbf{B} and the extrinsic curvature tensor. The extrinsic curvature corrections are out of the present analysis's scope and will be analyzed elsewhere. In the expression for A_a , $B_N = \mathbf{B} \cdot \mathbf{N}$ is the external magnetic field \mathbf{B} along the normal direction \mathbf{N} to the tangent plane at the fiducial point x' belonging to the surface patch.

1. The weak curvature regime

Our starting point is to consider that, for a surface with metric g_{ij} , the Riemann curvature tensor can be written as $R_{mklj} = \frac{R}{2} (g_{ml} g_{kj} - g_{mj} g_{kl})$, thus the Riemann curvature tensor and the spin connection can be written at the fiducial point x' as

$$\begin{aligned} R_{mklj} &= \frac{R}{2} (\delta_{ml} \delta_{kj} - \delta_{mj} \delta_{kl}) = \frac{R}{2} \epsilon_{mk} \epsilon_{lj} \\ \Omega_j &= i \xi \frac{R}{8} y^l \epsilon_{lj} \sigma_3, \text{ here } i = \sqrt{-1} \end{aligned} \quad (15)$$

and we can rewrite the ∇ operator as

$$\nabla_l = i \left(\frac{1}{\hbar} \boldsymbol{\pi}_l - i \Omega_l \right), \quad (16)$$

where $\boldsymbol{\pi}_l$ is the canonical momentum with the Pierls substitution using B_N instead of B . Thus, from Eqs. (13), (14), (15), and (16), we obtain that

$$\begin{aligned} \tilde{\mathcal{H}}_F^2 &= \frac{1}{\hbar^2} \boldsymbol{\pi}_l g^{lj} \boldsymbol{\pi}_j - g^{lj} \Omega_l \Omega_j - \frac{i}{\hbar} (\boldsymbol{\pi}_l g^{lj} \Omega_j + \Omega_l g^{lj} \boldsymbol{\pi}_j) \\ &+ \frac{1}{12} R - \frac{\xi q}{2\hbar} \sigma_3 \epsilon_{ij} F^{ij}. \end{aligned} \quad (17)$$

Considering only the first-order expansion in R , we obtain a "Hamiltonian" $\tilde{\mathcal{H}}_\xi^2 = \hbar^2 v_F^2 \tilde{\mathcal{H}}_F^2 = \hat{H}_0 + \hat{H}_I$ such that $\hat{H}_0 = v_F^2 \boldsymbol{\pi}^2$ is the square flat graphene Hamiltonian, which corresponds to the square of (9) and the perturbative term

$$\hat{H}_I \approx \left(v_F^2 \frac{R}{6} L^2 + v_F^2 \hbar^2 \frac{R}{12} \right) \mathbb{1} + \xi \left(v_F^2 \hbar \frac{R}{4} L + e \hbar v_F^2 B_N \right) \sigma_3, \quad (18)$$

where $L = \epsilon_{ij} y^i p^j$ is an angular momentum operator like in two dimensions. It can be seen that the first term within the second parenthesis is a pseudo-Rashba effect, and the second term is similar to a type of Zeeman effect. In the weak approximation, we also have neglected terms such as $R B_N y^i y_i$, and $R B_N^2 (y^i y_i)^2$ coming from the first and third term of Eq. (17).

Note that for the valleys $K(K')$, the valley index must be $\xi = 1$ ($\xi = -1$) in Eq. (18), which turns on a change in the sign of the last two terms due to a change in the third term of Eq. (17). Taken into account this observation, the eigenvalues of $\hat{H}_{K(K')}$ are given by (see Appendix C1)

$$E_{n,m,\tau,\xi,\pm} = \pm \hbar \omega_c \sqrt{n + \frac{1}{2} + \bar{\eta} \frac{1 + \lambda m}{2} + \frac{\lambda}{3} \left(m^2 + \frac{1}{2} \right)}, \quad (19)$$

where we defined the cyclotron frequency, ω_c , using the equation

$$\hbar \omega_c \equiv \sqrt{2e \hbar v_F^2 B_N},$$

the pseudomagnetic field,

$$B_s \equiv \frac{\hbar |R|}{4e}, \quad (20)$$

and the ratio of the pseudo and real magnetic fields,

$$\lambda \equiv \text{sign}(R) \frac{B_s}{B_N},$$

where $n = 0, 1, 2, \dots$ is the radial quantum number. The pseudo-spin coupling index $\bar{\eta}$ is defined by

$$\bar{\eta} \equiv \xi \tau = \pm 1 \quad (21)$$

that contains spatial and reciprocal information through the valley index ξ and the pseudo-spin index $\tau = \pm 1$, which labels the eigenvalues of σ_3 .

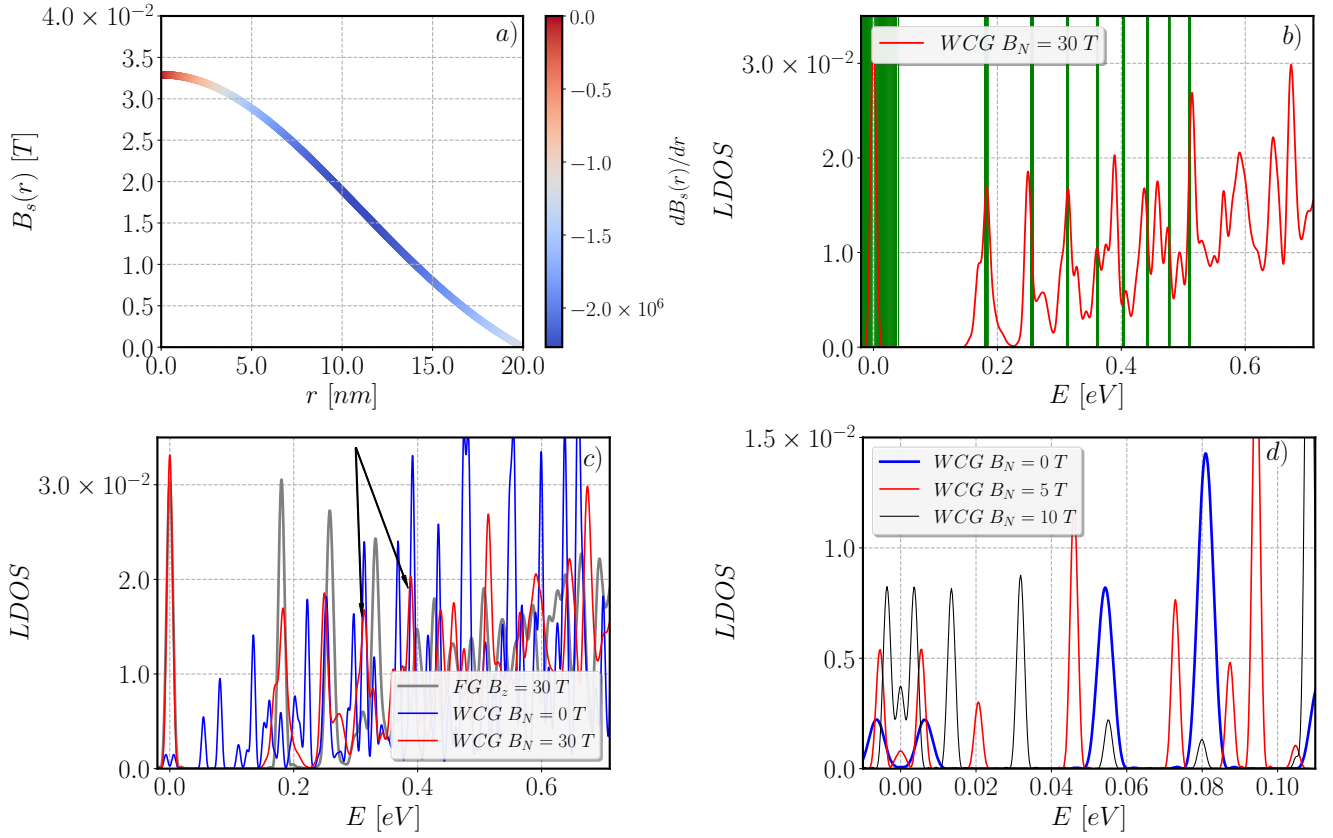


FIG. 3. Collection of plots for the weak pseudomagnetic field case for a graphene sheet with dimensions $L_x = L_y = 40$ nm; numerical comparison between the results obtained from the TB model and the Dirac model. a) Pseudomagnetic field profile obtained from a Gaussian deformation with parameters $z_0 = 4$ nm and $\varpi = 20$ nm. The most significant energy changes concerning flat graphene are produced by states close to the origin where $B_s \approx 0.033$ T. The color code of the curve indicates the field derivative, showing two separate regions as explained in the text. b) LDOS obtained from the LLs $|n| = 0, \dots, 7$ and $m_{max} = 11$ using the Dirac equation model in curved space with $B_{s,max} \approx 0.033$ T (see Eq. (19)), compared to the LDOS obtained from the TB model. Observe how the continuous model predicts almost all of the prominent peaks for low energies. c) LDOS obtained from the TB model for three representative cases, flat graphene under a very strong magnetic field ($B_N = 30T$) (gray lines), weak curvature regime under the same external magnetic field (red lines) and without the external magnetic field (blue lines). The contribution associated with the curvature is visible in the peaks indicated by arrows, which are shifted with respect to the flat graphene peaks. d) Zoom near $E = 0$, showing the evolution of the LDOS as the inversion symmetry is broken by a gradual increase of the external magnetic field. Notice how Landau levels with $n = 0$ arise as the temporal inversion is broken. In all cases, the plots are exclusively presented for $E > 0$ as the LDOS is symmetric with respect to the zero energy.

The quantum number m gives the splitting of each LL according to $m = -m_{max}, \dots, m_{max}$. As follows from the work by Ruiz et. al. [40], $m_{max} = \lfloor e(B_N + B_s)S/2\pi\hbar \rfloor$. If l is the angular momentum quantum number, then $m = l - n$.

In Fig. 3 a), we show the pseudomagnetic field profile for a Gaussian bump defined by the height function (A11) with parameters $z_0 = 4$ nm, $\varpi = 20$ nm. We observe that the states near the origin make the most significant contributions to the energy change compared to flat graphene. Therefore, in Fig. 3 b), we compare the LLs obtained from the TB model (4) with those from the Curved Dirac model (cf. Eq. (19)). For this case, we have considered the first $|n| = 0, \dots, 6$ levels, and the degeneracy number is $m_{max} = 2$. This degeneracy is visible for energy $E \approx 0$. It is important to note that the

contribution associated with the curvature is evident in the peaks indicated by the arrows in Figure 3 c). These peaks are observed to be shifted compared to the peaks of flat graphene.

2. The strong curvature regime

In the strong curvature corrugation approach, a quadratic shape of the local geometry is still maintained so that the Hamiltonian operator (13), with an external

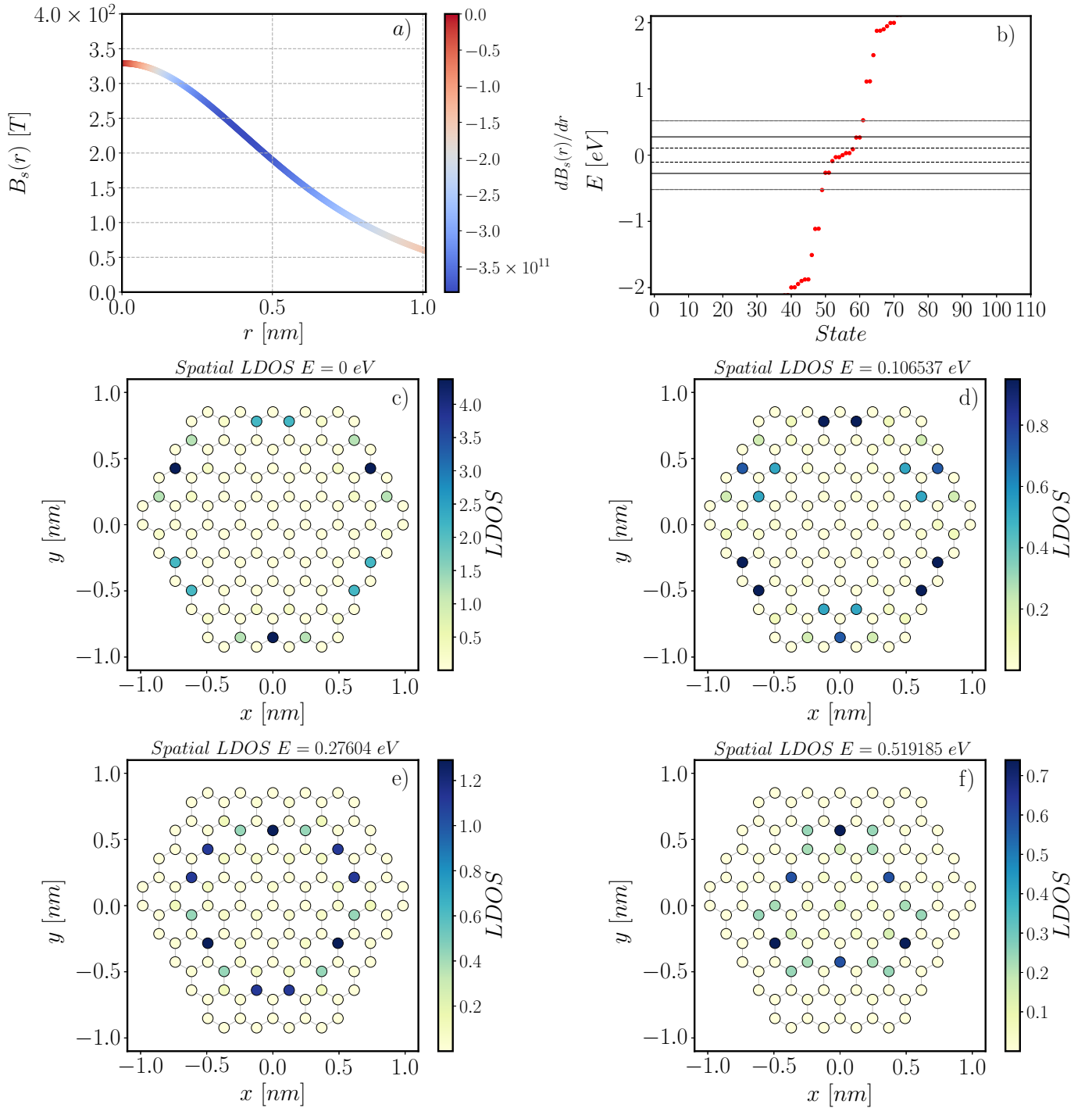


FIG. 4. Collection of plots for the strong pseudomagnetic field case for a graphene sheet with dimensions $L_x = L_y = 2$ nm; numerical comparison between the results obtained from the TB model and the Dirac model. a) The pseudomagnetic field profile B_s is shown as a function of radial distance r . b) The red dots are the energy of the states for the graphene nanodisk deformed by a Gaussian bump with parameters $z_0 = 4$ nm and $\varpi = 2$ nm obtained using the TB model under magnetic field $B_N = 30$ T. Additionally, the horizontal lines represent the eigenvalues obtained using the Dirac model Eq. (28). The dashed lines correspond to $\tau = -1$ while the solid lines represent $\tau = 1$. c), d), e), and f) are panels of the graphene nanodisk corresponding to energy values of the LDOS $E = 0$ eV, $E = 0.106537$ eV, $E = 0.27604$ eV and $E = 0.51985$ eV, respectively.

magnetic field, is reduced to

$$\begin{aligned} \tilde{\mathcal{H}}_F^2 = & \delta^{ij} \left(\frac{\pi_i}{\hbar} + \xi \frac{R}{8} \epsilon_{il} y^l \sigma_3 \right) \left(\frac{\pi_j}{\hbar} + \xi \frac{R}{8} \epsilon_{jk} y^k \sigma_3 \right) \\ & - \frac{R}{6\hbar^2} \epsilon_{ik} \epsilon_{lj} p^i y^k y^l p^j + \frac{R}{12} + \xi \frac{e}{\hbar} B_N \sigma_3, \end{aligned} \quad (22)$$

where the second term can be simplified after using the commutation relation $[y^l, p^j] = i\hbar\delta^{lj}$, that is,

$$\epsilon_{ik} \epsilon_{lj} p^i y^k y^l p^j = -L^2, \quad (23)$$

with $L = \epsilon_{ij} y^i p^j$ a two-dimensional angular momentum like operator. Clearly, $\tilde{\mathcal{H}}_\xi^2$ can be written as

$$\tilde{\mathcal{H}}_\xi^2 = v_F^2 \begin{pmatrix} \hat{h}_{\tau_R}^2 & 0 \\ 0 & \hat{h}_{-\tau_R}^2 \end{pmatrix}, \quad (24)$$

with

$$\hat{h}_{\tau_R}^2 = \delta^{ij} \hat{\Pi}_i^{(\tau_R)} \hat{\Pi}_j^{(\tau_R)} + \frac{R}{6} \left(\hat{L}^2 + \frac{\hbar^2}{2} \right) + \tau_R \text{sign}(R) e \hbar B_N, \quad (25)$$

where

$$\hat{\Pi}_i^{(\tau_R)} = \hat{p}_i + \frac{e}{2} B_T^{(\tau_R)} \epsilon_{li} y^l. \quad (26)$$

The total effective magnetic field is given by the sum of the external magnetic field B_N and its pseudomagnetic counterpart B_s ,

$$B_T^{(\tau_R)} \equiv B_N + \tau_R B_s, \quad (27)$$

where we defined the factor $\tau_R \equiv \bar{\eta} \text{sign}(R) = \pm 1$. Here recall $\bar{\eta}$ is the pseudo-spin coupling index (Eq. (21)), which is the product of the pseudo-spin index, τ , and the valley index, ξ . Notice that such effective fields and the valley-dependent Landau levels have been recently measured in graphene with a nanoscale ripple under an external magnetic field [94].

Therefore, the eigenvalues of $\tilde{\mathcal{H}}_{K(K')}$ are given by (see Appendix C 2),

$$\begin{aligned} E_{n,m,\tau,\xi,\pm} = & \pm \hbar \omega_{c,\tau_R} \\ & \times \left[n_{\tau_R} + \frac{1}{2} + \frac{\lambda_{\tau_R}}{3} \left(m_{\tau_R}^2 + \frac{1}{2} \right) + \bar{\eta} \Theta_{\tau_R} \right]^{1/2}, \end{aligned} \quad (28)$$

where now we have two possible cyclotron frequencies depending on the value of τ_R ,

$$\hbar \omega_{c,\tau_R} \equiv \sqrt{2e\hbar v_F^2 |B_T^{(\tau_R)}|}, \quad m_{\tau_R} = l_{\tau_R} - n_{\tau_R}. \quad (29)$$

We also defined,

$$\begin{aligned} \lambda_{\tau_R} = & \text{sign}(R) \frac{B_s}{|B_T^{(\tau_R)}|} \\ \Theta_{\tau_R} = & \frac{B_N}{2|B_T^{(\tau_R)}|} \end{aligned} \quad (30)$$

and $m_{\tau_R} = -m_{\max,\tau_R}, \dots, m_{\max,\tau_R}$.

As follows from the work of Ruiz et. al. [40],

$$m_{\max,\tau_R} = \frac{e|B_T^{(\tau_R)}|S}{2\pi\hbar}. \quad (31)$$

The pseudomagnetic field B_s definition is the same as in Eq. (20). Note that as stated below Eq. (52), the occupation number is inversely proportional to $|B_T^{(\tau_R)}|S$ while m_{\max,τ_R} is proportional. Thus, by changing the curvature values R and/or the area S , we will have a different eigenvalue behavior.

Specifically, employing a Gaussian bump deformation results in regions with curvatures of different signs. Consequently, the eigenvalues of these distinct regions become mixed. To effectively compare our Dirac model with the TB model, it is advisable to focus on a section of the material corresponding to a domain exhibiting the highest curvature.

In Figure 4, we consider a Gaussian deformation of the graphene sheet with parameters $z_0 = 4$ nm and $\varpi = 2$ nm. The condition for the biggest curvature is a region of radius 1 nm around the bump center. In subfigure 4 a), two spatial regions are established for the pseudomagnetic field B_s as a function of the radial distance r from the bump center. The region near the origin exhibits $B_s \approx 330$ T while the region near the edge has $B_s \approx 60$ T.

Once the biggest curvature region is identified, we proceed to compare the pseudomagnetic model with the TB calculation. In subfigure 4 b), the red dots are the energies obtained by using the TB model (4) in a graphene nanodisk of radius 1 nm. States with zero energy are attributed to edge states due to the zigzag configuration of the boundary, as shown in 4 c) and are not obtained from the Dirac model. States obtained from the TB with energies $E \approx 0.1065$ eV and $E \approx 0.2760$ eV correspond to the Dirac model LLs $n_{\tau_R=\mp 1} = 0$ with $B_s = 60.75$ T (represented by horizontal black lines), respectively (see Eq. (28)). These states are localized near the region edges, as shown in d) and e). Finally, states with $E \approx 0.5191$ eV correspond to the LLs $n_{\tau_R=\pm} = 0$ with $B_s = 329.10$ T (gray lines, see Eq. (28)). These states are localized near the origin, as demonstrated in panel f).

Unlike the real magnetic field, the pseudomagnetic field has an opposite sign at each Dirac valley due to the time-reversal symmetry. Consequently, in the presence of both uniform real and pseudo fields, it is expected that the LLs will lose their valley degeneracy [44, 45]. This is supported by Eq. (28) where the pseudospin coupling index is given by $\bar{\eta}$, showing that for $B_N \neq 0$, different sequences of energies are obtained. In the case of $B_N = 0$, Eq. (28) indicates the restoration of valley degeneracy as expected. Interestingly, for the case of flat graphene under a real magnetic field $B_N \neq 0$, the field shifts the LL sequences on each valley in a different fashion for each sublattice, i.e., zero energy solutions on different valleys have different pseudospin polarizations. However, the shift of the squared energy is precisely given by the difference between LL squared energies, resulting only in

a relabeling of the whole sequence, which turns out to be independent of the valley. Another way to understand this fact is to observe that in flat graphene under a real magnetic field, there is a Zeeman effect produced by the electron orbital motion [95]. This results in the widely known and experimentally observed zero mode LLs.

Before leaving this section, we emphasize that the existence of LLs induces changes in electronic properties and transport, leading to an electronic confinement effect, as has been observed in previous works [67–69].

IV. THE DHVA EFFECT ON FLAT GRAPHENE

Here, we review how the dHvA effect is obtained in flat graphene at the low-temperature limit $T \rightarrow 0$ K. In the first subsection, we establish the techniques needed, especially to compare them later with the curved situation. In the second subsection, we calculate the free energy, magnetization, and magnetic susceptibility of the flat graphene.

A. The Helmholtz free energy for a relativistic gas

To establish the dHvA effect in flat and curved situations, we compute the magnetization M . This is done by first obtaining the Helmholtz free energy per unit area, \mathcal{F} , which is given by

$$\mathcal{F}(\mu, \rho) = \Omega(\mu, T) + \mu\rho, \quad (32)$$

where μ refers to the chemical potential, ρ is the electron concentration in the graphene sheet, and $\Omega(\mu, T)$ is the thermodynamic potential. We should be careful at this point because the expression for $\Omega(\mu, T)$ needs to include considerations of the relativistic invariance of the Dirac equation. Indeed the adequate expression must read [22, 95, 96]

$$\Omega(\mu, T) = -k_B T \int_{-\infty}^{\infty} d\varepsilon \mathcal{D}(\varepsilon) \ln \left[2 \cosh \left(\frac{\varepsilon - \mu}{2k_B T} \right) \right], \quad (33)$$

where $\mathcal{D}(\varepsilon)$ is the total density of states (DOS) of graphene at finite temperature T , being k_B the Boltzmann constant. It encompasses information related to impurity scattering, electron-electron interactions, and electron-phonon interactions. Due to these interactions, the LLs undergo broadening, and the delta function must be substituted with a Lorentzian function to account for the broadening induced by such interactions. Then, the magnetization per unit area can be calculated by using one of the following expressions, [97, 98]

$$\begin{aligned} M &= - \left(\frac{\partial \mathcal{F}}{\partial B} \right)_{\rho, T}, \\ M &= - \left(\frac{\partial \Omega}{\partial B} \right)_{\mu, T}. \end{aligned} \quad (34)$$

In the first case, when ρ is constant, μ oscillates as a function of B ; while in the other case [22], $\partial \Omega(\mu, T) / \partial \mu = -\rho$.

Here, we discuss only the dHvA effect in the fixed electron density case ρ . Thus, we consider a system of N electrons within a sample area S moving in the magnetic induction field \mathbf{B} . Let the system remain at $T = 0$ K, and accordingly, the full occupation of LLs obeys [3, 5, 13]

$$g(B) \sum_{n=0}^{n_f} f_n = g(B)(n_f + 1) = \rho, \quad (35)$$

where n_f is the highest occupied LL, $f_n = [1 + \exp(\beta(\varepsilon_n - \mu))]^{-1}$ is the Fermi-Dirac distribution, $g(B) = g_s g_v B / \Phi_0$ is the degeneracy of the LLs, $g_s (g_v) = 2$ is the spin (valley) degeneracy. We use this relation to obtain

$$g(B) = \frac{2eB}{\hbar\pi}. \quad (36)$$

In the following, we provide an approximation to the thermodynamic potential $\Omega(\mu, T)$ in the limit when $T \rightarrow 0$ K. Let us consider the integration domain in Eq. (33) as the union of the intervals $I_- = (-\infty, \mu)$ and $I_+ = (\mu, \infty)$. For the sake of simplicity, $\mu > 0$; thus, in the zero temperature limit, one has $2 \cosh \left(\frac{\varepsilon - \mu}{2k_B T} \right) \simeq \frac{\mu - \varepsilon}{2k_B T}$ in I_- whereas $2 \cosh \left(\frac{\varepsilon - \mu}{2k_B T} \right) \simeq \frac{\varepsilon - \mu}{2k_B T}$ in I_+ . Therefore, one has the following expression for the thermodynamical potential,

$$\begin{aligned} \Omega(\mu, T = 0 \text{ K}) &= \frac{1}{2} \int_{-\infty}^{\mu} d\varepsilon \mathcal{D}_0(\varepsilon) (\varepsilon - \mu) \\ &\quad - \frac{1}{2} \int_{\mu}^{\infty} d\varepsilon \mathcal{D}_0(\varepsilon) (\varepsilon - \mu) \end{aligned} \quad (37)$$

where $\mathcal{D}_0(\varepsilon)$ is the DOS in the absence of scattering. We perform a further separation of the integration domain as $(-\infty, 0) \cup (0, \mu)$ in the first integral of last Eq. (37), and we add and subtract the integral $\frac{1}{2} \int_0^{\mu} d\varepsilon \mathcal{D}_0(\varepsilon) (\varepsilon - \mu)$. Thus

$$\begin{aligned} \Omega(\mu, T = 0 \text{ K}) &= \frac{1}{2} \int_{-\infty}^0 d\varepsilon \mathcal{D}_0(\varepsilon) (\varepsilon - \mu) \\ &\quad - \frac{1}{2} \int_0^{\infty} d\varepsilon \mathcal{D}_0(\varepsilon) (\varepsilon - \mu) \\ &\quad + \int_0^{\mu} d\varepsilon \mathcal{D}_0(\varepsilon) (\varepsilon - \mu). \end{aligned} \quad (38)$$

Now we take advantage of the evenness of the DOS, $\mathcal{D}_0(-\varepsilon) = \mathcal{D}_0(\varepsilon)$ to make a change of variable $\varepsilon \rightarrow -\varepsilon$. Thus the first integral turns out as $-\frac{1}{2} \int_0^{\infty} d\varepsilon \mathcal{D}_0(\varepsilon) (\varepsilon + \mu)$, implying the cancellation of the μ term from the first and second integrals. This procedure can also be implemented for the $\mu < 0$ case. The result is given by,

$$\Omega(\mu, T = 0 \text{ K}) = - \int_0^{\infty} d\varepsilon \mathcal{D}_0(\varepsilon) \varepsilon + \int_0^{|\mu|} d\varepsilon \mathcal{D}_0(\varepsilon) (\varepsilon - |\mu|) \quad (39)$$

This result is consistent with the treatment performed in other works [7, 22]. As the DOS is given by

$$\mathcal{D}_0(\varepsilon) = g(B) \sum_{n \in \mathbb{Z}} \delta(\varepsilon - \varepsilon_n) \quad (40)$$

the thermodynamical potential can be written as,

$$\Omega(\mu, T = 0 \text{ K}) = - \sum_{n=0}^{\infty} g(B) \varepsilon_n + \sum_{n=0}^{n_f} g(B) (\varepsilon_n - |\mu|) \quad (41)$$

This equality follows because, for a given B at zero temperature, the chemical potential is a constant equal to the highest LL energy ε_{n_f} . Now, from Eqs. (10), (32), (35) and (39), we obtain that \mathcal{F} is simply the total energy of the system per unit area up to the highest LL

$$\mathcal{F} = \sum_{n=-\infty}^{n_f} g(B) \varepsilon_n. \quad (42)$$

B. Revisiting the dHvA effect on flat graphene at $T = 0 \text{ K}$

According to the preceding subsection for a given B , the chemical potential is equal to the highest LL energy ε_{n_f} , thus for the flat graphene one has $\mu = \varepsilon_{n_f} = \sqrt{2e\hbar v_F^2 B n_f}$, and the Helmholtz free energy per unit area \mathcal{F} , due to a magnetic field, is, from Eqs. (35), (36),

$$\mathcal{F} = \sum_{n=-\infty}^{\lfloor \frac{\hbar\pi\rho}{2eB} - 1 \rfloor} \left(\frac{2eB}{\hbar\pi} \right) \left(\text{sign}(n) \sqrt{2e\hbar v_F^2 B |n|} \right) \quad (43)$$

with $\lfloor \cdot \rfloor$ denotes the floor function.

We define $B_0 \equiv \hbar\pi\rho/2e$, $\hbar\omega_{c0} \equiv \sqrt{2e\hbar v_F^2 B_0}$, $\hbar\omega_c \equiv \sqrt{2e\hbar v_F^2 B}$, and $\Lambda = B/B_0$, where B_0 is the value of B above which $n_f = 0$, i.e. only the valence levels are occupied, and ω_c (ω_{c0}) is the frequency of the cyclotron associated with the induction magnetic field B (B_0). From Eq. (43) we obtain a simplified free energy,

$$\mathcal{F} = \rho \hbar\omega_{c0} \Lambda^{3/2} \sum_{n=-\infty}^{\lfloor \frac{1}{\Lambda} - 1 \rfloor} \text{sign}(n) \sqrt{|n|} \quad (44)$$

The previous series can be expressed using the Riemann zeta function, ζ_R , and the Hurwitz zeta function, ζ_H . Hence, according to the procedure detailed in Appendix D,

$$\frac{\mathcal{F}}{\hbar\omega_{c0}\rho} = \mathfrak{F}_0(\Lambda, 0, 1), \quad (45)$$

where the function $\mathfrak{F}_0(\lambda, \Delta, \bar{f})$ is given by Eq. (D3) of Appendix D. In Fig. 5 a), we present a plot of \mathcal{F} calculated from Eq. (45). We obtain the magnetization per unit area using the above equation (45),

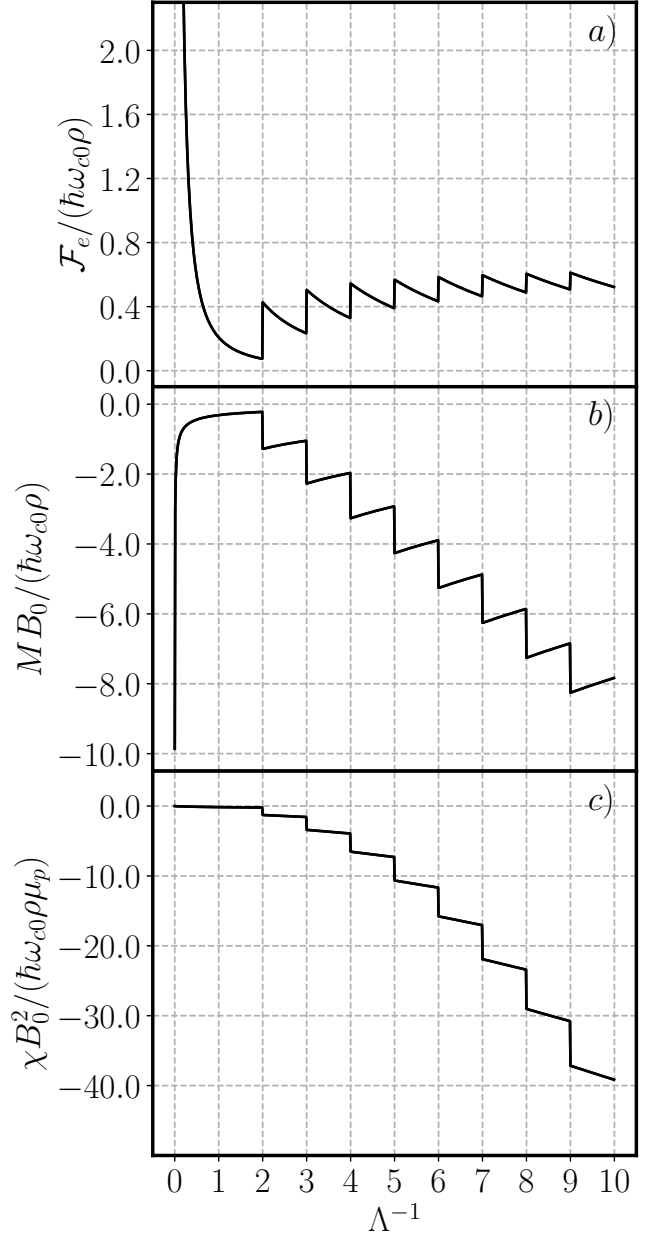


FIG. 5. Dimensionless plots of a) the Helmholtz free energy, obtained using Equation (45), b) the magnetization, obtained from Equation (46), and c) the magnetic susceptibility, obtained from Equation (47), as a function of the dimensionless parameter $\Lambda^{-1} = \frac{B_0}{B}$. These plots reveal the periodicity in $1/B$, as established by Onsager [26], demonstrating the dHvA effect. Additionally, they illustrate the susceptibility's divergence as $\Lambda^{-1} \rightarrow \infty$, corresponding to $B \rightarrow 0$ [22].

$M \equiv -(\partial\mathcal{F}/\partial B)|_{\rho, T}$, thus following discussion in Appendix D we obtain for the magnetization

$$\frac{B_0}{\hbar\omega_{c0}\rho} M = \mathfrak{M}_0(\Lambda, 0, 1), \quad (46)$$

where the function $\mathfrak{M}_0(\lambda, \Delta, \bar{f})$ is given in Appendix D given by Eq. (D5). Fig. 5 b) presents a plot of Eq. (46) showing the typical oscillations of the magnetization M

as a function of $1/B$. Increased temperature, impurity scattering, electron-electron interactions, and electron-phonon interactions cause the Landau Levels (LLs) to broaden. Consequently, the magnetization oscillation becomes less sharp [7, 22].

Let us now symbolize $\mathbf{B} = \mu_p \mathbf{H}$ and $B_0 = \mu_p H_0$, μ_p as being the magnetic permeability of free space, \mathbf{H} stands for the magnetic field intensity. Thus, we obtain that the magnetic susceptibility per unit area, $\chi \equiv (\partial M / \partial H)$, is

$$\frac{B_0^2}{\hbar \omega_{c0} \rho \mu_p} \chi = \mathfrak{S}_0(\Lambda, 0, 1), \quad (47)$$

where the function $\mathfrak{S}_0(\lambda, \Delta, \bar{f})$ is given in Appendix D by Eq. (D6). As seen in Fig. 5 c), the dependence $\sim \sqrt{B}$ of the magnetization implies that the susceptibility $\chi \propto B^{-1/2}$ diverges at zero field, a result similar to that obtained by Sergei G. Sharapov and his collaborators two decades ago [22]. Experimentally, measuring such a striking result proves challenging due to the weak signal in monolayers and the effect of temperature and disorder [73]. The experimental magnetization was found to be aligned with the predicted dependence for the Dirac spectrum, but the doping level remained elusive [99]. In another study, isolating the residual contribution of paramagnetic spins proved unattainable [24, 100]. More recently, Vallejo Bustamante et al. managed to capture signatures of such susceptibility divergence by placing two giant magnetoresistance detectors below a sample of graphene sandwiched by layers of hexagonal boron nitride [73]. Note the strong diamagnetic character of graphene in Fig. 5 c) at low temperatures, as confirmed in an experiment with graphene nanocrystals obtained by sonic exfoliation [99].

V. DHVA EFFECT PRODUCED BY A REAL MAGNETIC FIELD IN CURVED GRAPHENE.

In this section, we will discuss the dHvA effect in strongly curved graphene with a fixed electron density ρ . To do so, as mentioned earlier in Sec. IV A, it is necessary to first compute the Helmholtz free energy by summing the energy for each filled level. For this purpose, it is possible to employ a generalization of the Euler-Maclaurin formula to perform the double sums. However, it is advisable to make certain considerations that allow us to simplify the calculation. In particular, motivated by experimental findings in freestanding graphene, which reports values for the pseudomagnetic field ranging from a few to tens of Tesla [101–103], we will consider the case of strongly curved graphene under a real magnetic field and the limit $|B_T^{(\tau_R)}| S < 2\pi\hbar/e$. Therefore, $m_{max} = \left[e B_T^{(\tau_R)} S / 2\pi\hbar \right] = 0$ (see the corresponding effects on the LDOS in Fig. 4 when $B_s \gg B_N$). Note that in recent experiments employing trilayer graphene encapsulated with hBN it has been possible to obtain pseudomagnetic fields on the order of millitesla [53], i.e., within the weak curvature regime. However, this type

of system extends beyond the scope of what we have assumed in this work and will be explored in future studies due to its relevance.

Thus, in the strongly curved graphene limit and from Eq. (28), the eigenvalues can be rewritten only in terms of the principal quantum number, n , the pseudo-spin coupling index $\bar{\eta}$ and the curvature R , as

$$E_{n, \bar{\eta}, \pm}(R) = \pm \hbar \omega_{c, \tau_R} \sqrt{n + \Delta_{\bar{\eta}}(R)}, \quad n \geq n_0^{\bar{\eta}}, \quad (48)$$

where the cyclotron frequency is obtained from $\hbar \omega_{c, \tau_R} = \sqrt{2e\hbar v_F^2 |B_T^{(\tau_R)}|}$, and the gap-like term, $\Delta_{\bar{\eta}}(R)$, is given by

$$\Delta_{\bar{\eta}}(R) \equiv \frac{1}{2} + \frac{\text{sign}(R)}{6} \left(\frac{B_s + 3 \text{sign}(R) \bar{\eta} B_N}{|B_N + \text{sign}(R) \bar{\eta} B_s|} \right). \quad (49)$$

From the energy eigenvalues (48), the lowest value of n is $n_0^{\bar{\eta}} \equiv \lceil -\Delta_{\bar{\eta}}(R) \rceil$, such that the LLs corresponding to $n < n_0^{\bar{\eta}}$ are not longer eigenstates as the pseudomagnetic field breaks the inversion symmetry and opens a gap. In other words, the primary effect of the curvature is to shift the Landau Level (LL) sequence and induce a gap at the zero level when $\Delta_{\bar{\eta}}(R) \geq 0$. In Fig. 6, we present the size of this gap term as a function of B_s/B_N for different signs of the curvature and pseudo-spin coupling index $\bar{\eta}$. Asymptotically, when $B_s/B_N \rightarrow \infty$, $\Delta_{\bar{\eta}}(R)$ tends to Δ_R , with

$$\Delta_R \equiv \frac{1}{2} + \frac{1}{6} \text{sign}(R), \quad (50)$$

recovering the previous result [40]. Meanwhile, in the limit $B_s/B_N \rightarrow 0$, then $\Delta_{\bar{\eta}}(R) \rightarrow \frac{1}{2}(1 + \bar{\eta})$ analogous to a pseudo-Zeeman term, recovering the result for the flat graphene. It is noteworthy that $\Delta_{\bar{\eta}}(R)$ is not well defined when $B_s/B_N = 1$ and $\tau_R = -1$ because there is a resonance effect between the pseudo and external magnetic fields. Also, $\Delta_{\bar{\eta}}(R > 0)$ changes sign when $B_s/B_N < 3/2$.

To calculate the free energy, we consider a system containing N electrons within a sample of area S in the low-temperature approximation, $T \approx 0$ K. This approximation is valid because, from Eq. (29), the characteristic temperature T_R associated with the cyclotron frequency is

$$T_R = \hbar \omega_{c, \tau_R} / k_B \sim 10^3 \text{ K}, \quad (51)$$

for a field of $B_T^{(\tau_R)} \sim 3 \times 10^2 \text{ T}$ [40, 104]. Beyond this temperature, the approximation $T \rightarrow 0$ K is no longer applicable. The full occupation of LLs obeys,

$$\begin{aligned} \rho &= \sum_{\bar{\eta}=\pm 1} \sum_{n=n_0^{\bar{\eta}}}^{n_{\bar{\eta}, f}} g_{\bar{\eta}}(B_N, B_s) f_n, \\ &= \sum_{\bar{\eta}=\pm 1} g_{\bar{\eta}}(B_N, B_s) (n_{\bar{\eta}, f} + 1 - n_0^{\bar{\eta}}), \end{aligned} \quad (52)$$

where f_n is the Fermi-Dirac distribution, which at low-temperature regime is $f_n \approx 1$, $n_{\bar{\eta}, f}$ is the highest LL

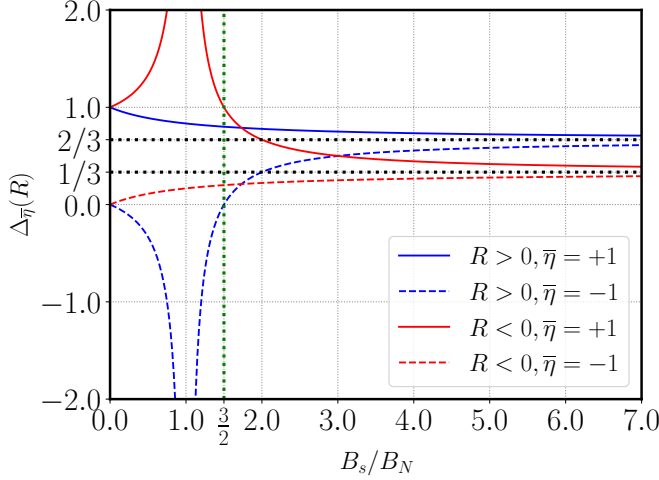


FIG. 6. Plot of the gap-like term $\Delta_{\bar{\eta}}(R)$ (See Eq. (49)). The blue and red solid (dashed) lines correspond to $R > 0, \bar{\eta} = 1$ ($R > 0, \bar{\eta} = -1$) and $R < 0, \bar{\eta} = 1$ ($R < 0, \bar{\eta} = -1$), respectively. Asymptotically, when $B_s/B_N \rightarrow \infty$ then $\Delta_{\bar{\eta}}(R)$ tends to Δ_R . Meanwhile, in the limit $B_s/B_N \rightarrow 0$ then $\Delta_{\bar{\eta}}(R) \rightarrow \frac{1}{2}(1 + \bar{\eta})$ analogous to a pseudo Zeeman term in flat graphene.

occupied per pseudo-spin coupling index, and the degen-

$$\mathcal{F}_e = \sum_{\bar{\eta}=\pm 1} \sum_{n=n_0^{\bar{\eta}}}^{\infty} g_{\bar{\eta}}(B_N, B_s) E_{n, \bar{\eta}, -}(R) + \sum_{\bar{\eta}=\pm 1} \sum_{n=n_0^{\bar{\eta}}}^{n_{\bar{\eta}, f}} g_{\bar{\eta}}(B_N, B_s) E_{n, \bar{\eta}, +}(R) \quad (56)$$

$$= \sum_{\bar{\eta}=\pm 1} \hbar \omega_{c, \tau R} g_{\bar{\eta}}(B_N, B_s) \sum_{n=-\infty}^{n_{\bar{\eta}, f} - n_0^{\bar{\eta}}} \text{sign}(n) \sqrt{|n| + n_0^{\bar{\eta}} + \Delta_{\bar{\eta}}(R)}, \quad (57)$$

with the highest LL occupied $n_{\bar{\eta}, f}$ calculated using equation (52) and the highest LL condition $E_{x, +, +}(R) = E_{y, -, +}(R)$ using Eq. (48), where $x \equiv n_{+, f}$ and $y \equiv n_{-, f}$. Indeed, after a straightforward calculation using this procedure, the highest LL are obtained by

$$n_{\bar{\eta}, f} = \left\lfloor \frac{1}{\tilde{\Lambda}_{\bar{\eta}}} - f_{\bar{\eta}}(R) \right\rfloor, \quad (58)$$

where $\tilde{\Lambda}_{\bar{\eta}} \equiv |B_N + \text{sign}(R)\bar{\eta}B_s|/\tilde{B}_0$, being $\tilde{B}_0 \equiv \hbar\pi\rho/4e$, and

$$f_{\bar{\eta}}(R) \equiv \frac{1}{2} + \frac{B_{>} + \bar{\eta}B_N}{2(B_{>} + \text{sign}(R)\bar{\eta}B_{<})} - \frac{\sum_{\bar{q}=\pm 1} n_0^{\bar{q}}(B_{>} + \bar{q} \text{sign}(R)B_{<})}{2(B_{>} + \text{sign}(R)\bar{\eta}B_{<})}, \quad (59)$$

where $B_{<}(B_{>})$ is the smaller (larger) of B_s and B_N . Thus, we rewrite the electronic free energy in a very sim-

ilarity of the LLs is given by [40],

$$g_{\bar{\eta}}(B_N, B_s) = 2g_s |B_T^{(\tau R)}|/\Phi_0 = \frac{2e|B_N + \text{sign}(R)\bar{\eta}B_s|}{\hbar\pi}, \quad (53)$$

where g_s is the spin degeneracy and Φ_0 is the magnetic flux quantum.

The Helmholtz free energy per unit area, \mathcal{F} , opposite to the flat case, can be expressed as the sum of two parts,

$$\mathcal{F} = \mathcal{F}_e + \mathcal{W} \quad (54)$$

where \mathcal{F}_e is the electronic free energy part obtained using the electronic spectra (48), whereas \mathcal{W} is the elastic energy stored due to the geometrical deformation. On the one hand, \mathcal{W} per unit area is the mechanical work associated with the deformation part, and it can be expressed as [105, 106]

$$\mathcal{W} = \sigma_{ij} e_{ij}, \quad (55)$$

i.e., it is the contraction between the deformation tensor, e_{ij} and the stress tensor, σ_{ij} . On the other hand, the electronic part can be expressed as the sum of the correspondent electronic energy per pseudo-spin coupling index, $\mathcal{F}_e^{\bar{\eta}}$. Thus, from Eqs. (48) and (52), the electronic free energy is $\mathcal{F}_e \equiv \sum_{\bar{\eta}=\pm 1} \mathcal{F}_e^{\bar{\eta}}$, that is,

ilar form to the flat case as

$$\mathcal{F}_e = \frac{\rho}{2} \hbar \tilde{\omega}_{c0} \sum_{\bar{\eta}=\pm 1} \tilde{\Lambda}_{\bar{\eta}}^{3/2} \sum_{n=-\infty}^{n_{\bar{\eta}, f} - n_0^{\bar{\eta}}} \text{sign}(n) \sqrt{|n| + \Delta_{\bar{\eta}}(R) + n_0^{\bar{\eta}}}, \quad (60)$$

where $\hbar \tilde{\omega}_{c0} \equiv \sqrt{2e\hbar v_F^2 \tilde{B}_0}$. Hence, after using the procedure detailed in Appendix D, the electronic free energy is,

$$\frac{\mathcal{F}_e}{\hbar \tilde{\omega}_{c0} \rho} = \frac{1}{2} \sum_{\bar{\eta}=\pm 1} \mathfrak{F}_0 \left(\tilde{\Lambda}_{\bar{\eta}}, \Delta_{\bar{\eta}}(R), f_{\bar{\eta}}(R) \right), \quad (61)$$

where the function $\mathfrak{F}_0(\lambda, \Delta, \bar{f})$ is given in Appendix D.

In Fig. 7 a), we present the behavior of the free energy Eq.(61) as a function of the inverse real magnetic induction field with respect to the pseudomagnetic field. First, in Fig. 7 a), we observe oscillations that can be traced back to the interference between valleys. Secondly, there are critical values of B_s/B_N at which the free energy has

crossovers between negative and positive curvature cases. However, for $B_s \sim B_N$, the $R > 0$ case always has lower free energy, while for $B_s \gg B_N$, the reverse case is seen, i.e., the case $R < 0$ has lower free energy. Thus, Eq. (61) is consistent with known examples of graphitic surfaces with positive curvature as fullerenes [107, 108] or those with negative curvature like Schwarzites, proposed many years ago by Mackay and Terrones [107, 109–111] and other authors [112, 113].

To obtain the magnetization and magnetic susceptibility, we use the equations

$$M = - \left(\frac{\partial \mathcal{F}}{\partial B_N} \right)_{\mu, T, e_{ij}} = - \left(\frac{\partial \mathcal{F}_e}{\partial B_N} \right)_{\mu, e_{ij}} \quad (62)$$

$$\chi = \left(\frac{\partial M}{\partial H} \right)_{\mu, e_{ij}},$$

in particular, maintaining the deformation tensor, e_{ij} , constant. The resulting magnetization per unit area, M , depends whether B_s is bigger or smaller than B_N ; i.e.

a) in the case $B_s > B_N$,

$$\frac{\tilde{B}_0}{\hbar \tilde{\omega}_{c0} \rho} M = \frac{\text{sign}(R)}{2} \sum_{\bar{\eta}=\pm 1} \bar{\eta} \left[\mathfrak{M}_0(\tilde{\Lambda}_{\bar{\eta}}, \Delta_{\bar{\eta}}(R), f_{\bar{\eta}}(R)) + \frac{\text{sign}(R) B_s}{\tilde{B}_0} \mathfrak{M}_1(\tilde{\Lambda}_{\bar{\eta}}, \Delta_{\bar{\eta}}(R), f_{\bar{\eta}}(R)) \right], \quad (63)$$

b) in the case $B_N > B_s$,

$$\frac{\tilde{B}_0}{\hbar \tilde{\omega}_{c0} \rho} M = \frac{1}{2} \sum_{\bar{\eta}=\pm 1} \left[\mathfrak{M}_0(\tilde{\Lambda}_{\bar{\eta}}, \Delta_{\bar{\eta}}(R), f_{\bar{\eta}}(R)) + \frac{\text{sign}(R) B_s}{\tilde{B}_0} \mathfrak{M}_1(\tilde{\Lambda}_{\bar{\eta}}, \Delta_{\bar{\eta}}(R), f_{\bar{\eta}}(R)) \right], \quad (64)$$

where the functions $\mathfrak{M}_0(\lambda, \Delta, \bar{n}, \bar{f})$ and $\mathfrak{M}_1(\lambda, \Delta, \bar{n})$ are given in Appendix D. In Fig. 7 b), we present the behavior of the magnetization as a function of the inverse magnetic induction field.

In Fig. 7 c), we present the magnetic susceptibility, given by,

$$\frac{\tilde{B}_0^2}{\hbar \tilde{\omega}_{c0} \rho \mu_p} \chi = \frac{1}{2} \sum_{\bar{\eta}=\pm 1} \left[\mathfrak{S}_0(\tilde{\Lambda}_{\bar{\eta}}, \Delta_{\bar{\eta}}(R), f_{\bar{\eta}}(R)) + \mathfrak{S}_1 \left(\frac{\text{sign}(R) B_s}{\tilde{B}_0}, \tilde{\Lambda}_{\bar{\eta}}, \Delta_{\bar{\eta}}(R), f_{\bar{\eta}}(R) \right) \right], \quad (65)$$

where the functions $\mathfrak{S}_0(\lambda, \Delta, \bar{f})$ and $\mathfrak{S}_1(\mathbf{b}_1, \lambda, \Delta, \bar{f})$ are given in Appendix D.

As observed in Fig. 7 (b) and (c), the dependence of the magnetization on $\sim \sqrt{B_s + \text{sign}(R)\bar{\eta}B_N}$ implies that the susceptibility $\chi \sim (B_s + \text{sign}(R)\bar{\eta}B_N)^{-1/2}$ avoids the divergence problem that exists for a strictly flat sheet of graphene at zero value external magnetic field. It is

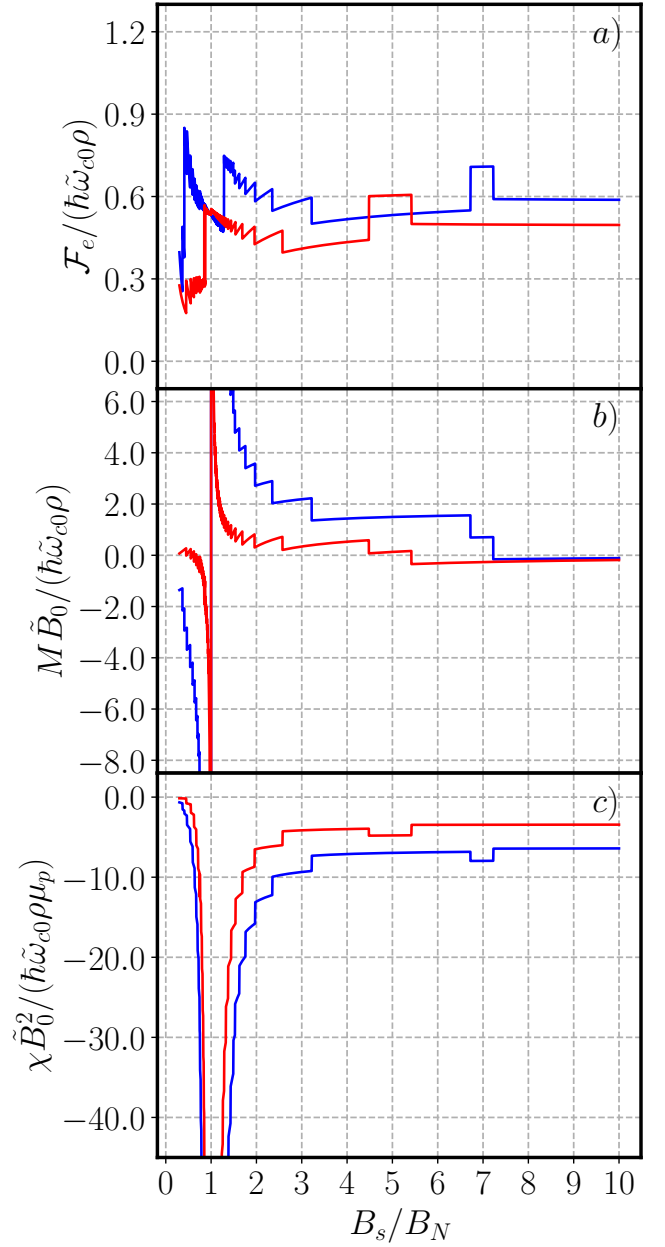


FIG. 7. Electronic part of the Helmholtz free energy (Eq. (61)), magnetization (Eq. (67)), and magnetic susceptibility (Eq. (69)) as a function of B_s/B_N for two different curvatures, $R > 0$ (blue lines) and $R < 0$ (red lines). Taking into account $\rho \sim 2 \times 10^{18} \text{ m}^{-2}$ [114], $B_s \sim 300 \text{ T}$ [104], and from Eq. $\tilde{B}_0 = \hbar \pi \rho / 4e \sim 1033.47 \text{ T}$, the magnetic susceptibility reaches a nearly constant value in weak magnetic fields $B_N \ll B_s$, due to the inclusion of the pseudomagnetic field. This prevents the theoretical issue of the diamagnetic divergence in flat graphene at low temperatures. On the other hand, for strong magnetic fields such that $B_s/B_N \rightarrow 1$, a resonance effect appears as the cyclotron frequency becomes $\omega_{\tau_R} = 0$ in one valley and $\omega_{\tau_R} = 2|B_N|^{1/2}$ in the other. This effect changes the magnetization from being negative to positive. However, the magnetic susceptibility is negative.

noteworthy that diamagnetism in graphene decreases as

the curvature increases. Therefore, corrugations appear to be essential for understanding experimentally measurable thermodynamic properties. In the literature, there are currently limited available results.

Interestingly, Fig. 7 shows a resonance effect for very strong magnetic fields such that $B_s/B_N \rightarrow 1$. To understand this, we observe that the susceptibility $\chi \sim (B_s + \text{sign}(R)\bar{\eta}B_N)^{-1/2}$, displays a singularity if $\text{sign}(R)\bar{\eta} = -1$. Therein, the magnetization changes from negative to positive values. The explanation of such phenomena is that the cyclotron frequency $\omega_{\tau R} \sim |B_N + \tau_R B_s|^{1/2}$ becomes zero for one valley implying the Landau Levels collapse to zero modes. In the other valley, $\omega_{\tau R} \sim |2B_N|^{1/2}$, implying that only one valley contributes to the free energy.

VI. THE EMERGENCE OF A PSEUDO-DHVA EFFECT PRODUCED BY CURVATURE WITHOUT REAL MAGNETIC FIELDS

In this section, we demonstrate how a pseudo-dHvA effect arises as a result of the mechanical properties of curved graphene. For this purpose, note that the treatment performed in Section V can be applied with the pseudomagnetic field and define the quantities $M_s \equiv -(\partial\mathcal{F}/\partial B_s)_\mu$ and $\chi_s \equiv (\partial M_s/\partial H_s)_\mu$ as the pseudomagnetization and pseudomagnetic susceptibility per unit area [2, 12], respectively. Here, $B_s = \mu_p H_s$ where H_s is a pseudo-magnetic field intensity.

In the case of curved graphene under a magnetic field B_N , the pseudo magnetization per unit area, M_s is given by the sum of an electronic pseudo magnetization part, M_{se} , and a pseudo magnetization part of the deformation, M_{sd} . The resulting pseudo magnetization per unit area, M , depends whether B_s is bigger or smaller than B_N ; i.e.

a) in the case $B_s > B_N$,

$$\frac{\tilde{B}_0}{\hbar\tilde{\omega}_{c0}\rho} M_{se} = \frac{1}{2} \sum_{\bar{\eta}=\pm 1} \left[\mathfrak{M}_0 \left(\tilde{\Lambda}_{\bar{\eta}}, \Delta_{\bar{\eta}}(R), f_{\bar{\eta}}(R) \right) - \frac{\bar{\eta}B_N}{\tilde{B}_0} \mathfrak{M}_1 \left(\tilde{\Lambda}_{\bar{\eta}}, \Delta_{\bar{\eta}}(R), f_{\bar{\eta}}(R) \right) \right], \quad (66)$$

b) in the case $B_N > B_s$,

$$\frac{\tilde{B}_0}{\hbar\tilde{\omega}_{c0}\rho} M_{se} = \sum_{\bar{\eta}=\pm 1} \frac{\text{sign}(R)\bar{\eta}}{2} \left[\mathfrak{M}_0 \left(\tilde{\Lambda}_{\bar{\eta}}, \Delta_{\bar{\eta}}(R), f_{\bar{\eta}}(R) \right) - \frac{\bar{\eta}B_N}{\tilde{B}_0} \mathfrak{M}_1 \left(\tilde{\Lambda}_{\bar{\eta}}, \Delta_{\bar{\eta}}(R), f_{\bar{\eta}}(R) \right) \right], \quad (67)$$

(see Eq. (D5)). The deformation pseudo magnetization part, M_{sd} , is not null since the stress tensor and

deformation tensor depend on the pseudomagnetic field, thus it is expressed as

$$M_{sd} = \left(\frac{\partial\mathcal{W}}{\partial B_s} \right) = \sigma_{ij} \left(\frac{\partial e_{ij}}{\partial B_s} \right) + e_{ij} \left(\frac{\partial \sigma_{ij}}{\partial B_s} \right). \quad (68)$$

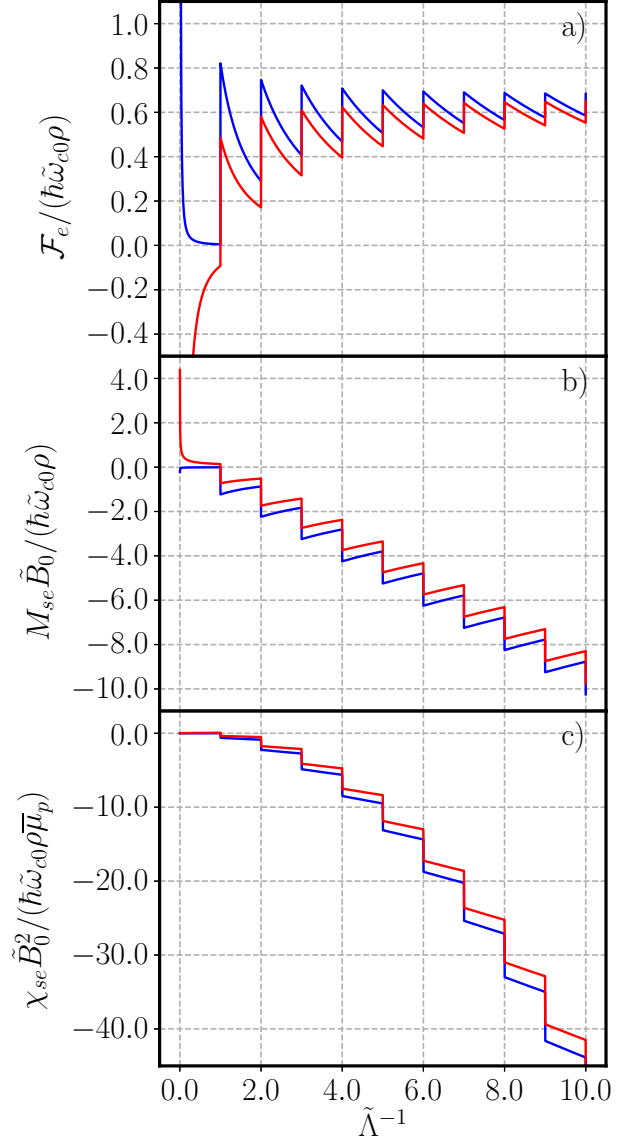


FIG. 8. Electronic part of a) the Helmholtz free energy (Eq. (61)), b) the pseudo magnetization (Eq. (67)), and c) the pseudomagnetic susceptibility (Eq. (69)) without a magnetic field, i.e. $B_N = 0$ T, as a function of $\tilde{\Lambda}^{-1} = \tilde{B}_0/B_s$, for two different curvatures $R > 0$ (blue lines) and $R < 0$ (red lines). As mentioned in Sec. VI, the pseudo magnetization is associated with a mechanical stress tensor, and the pseudo susceptibility with internal reaction forces that oppose deformation, thus the discontinuities of these forces with a period of $1/B_s$ give rise to a pseudo-de Haas van Alphen effect.

Similarly, the pseudo-susceptibility, χ_s , will be the sum of a part due to electronics χ_{se} and a part due to the

deformation χ_{sd} .

$$\frac{\tilde{B}_0^2}{\hbar\tilde{\omega}_{c0}\rho\mu_p}\chi_{se} = \frac{1}{2} \sum_{\bar{\eta}=\pm 1} \left[\mathfrak{S}_0 \left(\tilde{\Lambda}_{\bar{\eta}}, \Delta_{\bar{\eta}}(R), f_{\bar{\eta}}(R) \right) + \mathfrak{S}_1 \left(-\frac{\bar{\eta}B_N}{\tilde{B}_0}, \tilde{\Lambda}_{\bar{\eta}}, \Delta_{\bar{\eta}}(R), f_{\bar{\eta}}(R) \right) \right], \quad (69)$$

(see Eq. (D6)) and χ_{sd} is given by

$$\begin{aligned} \chi_{sd} &= 2 \left(\frac{\partial \sigma_{ij}}{\partial B_s} \right) \left(\frac{\partial e_{ij}}{\partial B_s} \right) + \sigma_{ij} \left(\frac{\partial^2 e_{ij}}{\partial B_s^2} \right) + e_{ij} \left(\frac{\partial^2 \sigma_{ij}}{\partial B_s^2} \right) \\ &= 2F_i \left(\frac{\partial B_s}{\partial y_j} \right)^{-1} \left(\frac{\partial e_{ij}}{\partial B_s} \right) + \sigma_{ij} \left(\frac{\partial^2 e_{ij}}{\partial B_s^2} \right) + e_{ij} \left(\frac{\partial^2 \sigma_{ij}}{\partial B_s^2} \right), \end{aligned} \quad (70)$$

where F_j is the force density acting on the material in the direction j . In the previous expression, we used the fact that [105, 106]

$$F_i = \partial \sigma_{ij} / \partial y_j \quad (71)$$

As seen in Fig. 8, we recover the divergence case when $B_N = 0$ and $B_s = 0$ (flat situation). However, it is necessary to note that this pseudo magnetization, M_{se} , and pseudo susceptibility, χ_{se} , are related to mechanical observables and arise from the electronic part, and as shown in Eq. (68), the pseudo magnetization of the deformation part is related to the stress tensor. From Eq. (69), the pseudo susceptibility is described by oscillating internal forces acting directly on the graphene sheet, resulting in a mechanically induced pseudo de Haas van Alphen effect (pseudo-dHvA). Therefore, electronic forces act on the graphene sheet opposing flatness when $B_N = 0$ and $B_s \rightarrow 0$. This means that spontaneous corrugations will appear to reduce the free energy. This is related to discussions in previous works on how graphene (without substrate) achieves mechanical equilibrium by corrugation [115–117].

As a further result, in the strong curvature regime, the electronic forces opposing deformation are smaller in negative curvature surfaces. This result is consistent with the numerical prediction by Terrones et al. concerning the stability of negative curved graphitic structures [110].

VII. PHYSICAL DIFFERENCES BETWEEN MAGNETIZATION AND PSEUDOMAGNETIZATION

In this section, we briefly discuss the physical difference between real magnetization and pseudo magnetization. To begin with, it is noteworthy to mention that magnetization represents the ratio of a change of free energy to a change in a real magnetic field, whereas pseudo-magnetization gives the ratio of the change of free energy to a change in a pseudomagnetic field. In other words, pseudo magnetization is related to how the free energy is modified when the curvature of the graphene sheet is changed. Indeed, from the quantitative viewpoint, let us

consider the case $B_s > B_N$. In this case, the magnetization per unit area can be obtained from Eq. (63) that can be rewritten exactly as

$$M = \text{sign}(R) [\tilde{\mu}_+(B_N, B_s) - \tilde{\mu}_-(B_N, B_s)], \quad (72)$$

where, we have defined $\tilde{\mu}_{\bar{\eta}}(B_N, B_s)$ as a magnetic-like moment given by

$$\tilde{\mu}_{\bar{\eta}}(B_N, B_s) = \tilde{\mu}_{\bar{\eta}}^{(0)}(B_N, B_s) + \frac{\text{sign}(R)B_s}{\tilde{B}_0} \tilde{\mu}_{\bar{\eta}}^{(1)}(B_N, B_s), \quad (73)$$

where

$$\begin{aligned} \tilde{\mu}_{\bar{\eta}}^{(0)}(B_N, B_s) &= \frac{\hbar\tilde{\omega}_{c0}\rho}{2\tilde{B}_0} \mathfrak{M}_0 \left(\tilde{\Lambda}_{\bar{\eta}}, \Delta_{\bar{\eta}}(R), f_{\bar{\eta}}(R) \right) \\ \tilde{\mu}_{\bar{\eta}}^{(1)}(B_N, B_s) &= \frac{\hbar\tilde{\omega}_{c0}\rho}{2\tilde{B}_0} \mathfrak{M}_1 \left(\tilde{\Lambda}_{\bar{\eta}}, \Delta_{\bar{\eta}}(R), f_{\bar{\eta}}(R) \right). \end{aligned} \quad (74)$$

Therefore, the magnetization M is given by an imbalance between the charge carriers with different $\bar{\eta}$. In contrast, using Eq. (66), the pseudo magnetization per area unit can be written exactly as

$$M_{se} = \tilde{\nu}_+(B_N, B_s) + \tilde{\nu}_-(B_N, B_s), \quad (76)$$

where $\tilde{\nu}_{\bar{\eta}}(B_N, B_s)$ as another magnetic-like moment given by

$$\tilde{\nu}_{\bar{\eta}}(B_N, B_s) = \tilde{\mu}_{\bar{\eta}}^{(0)}(B_N, B_s) - \bar{\eta} \frac{B_N}{\tilde{B}_0} \tilde{\mu}_{\bar{\eta}}^{(1)}(B_N, B_s). \quad (77)$$

Therefore, the pseudomagnetization M_{se} is given by the sum of the magnetic like-moments $\tilde{\nu}_{\bar{\eta}}(B_N, B_s)$ of charge carriers with different $\bar{\eta}$.

Next, we look at the difference between M and M_{se} in the approximation $B_s \gg B_N$. At first order in B_N/B_s , the arguments of \mathfrak{M}_0 and \mathfrak{M}_1 are,

$$\tilde{\Lambda}_{\bar{\eta}} \approx \frac{B_s}{\tilde{B}_0} \left(1 + \text{sign}(R)\bar{\eta} \frac{B_N}{B_s} \right), \quad (78)$$

$$\Delta_{\bar{\eta}}(R) \approx \Delta_R + \frac{1}{3}\bar{\eta} \frac{B_N}{B_s}, \quad (79)$$

$$f_{\bar{\eta}}(R) \approx 1 + \frac{1}{2}(1 - \text{sign}(R))\bar{\eta} \frac{B_N}{B_s}, \quad (80)$$

implying that in the limit when $B_N \rightarrow 0$ the time-reversal symmetry is restored, and the LLs are degenerated in pseudospin coupling index $\bar{\eta}$, since $\bar{\eta}$ appears as a coefficient in the term B_N/B_s . In addition, in this limit one has $\tilde{\mu}_+^{(k)}(B_N, B_s) = \tilde{\mu}_-^{(k)}(B_N, B_s)$, for $k = 0, 1$, $\tilde{\mu}_+(B_N, B_s) = \tilde{\mu}_-(B_N, B_s)$, and $\tilde{\nu}_+(B_N, B_s) = \tilde{\nu}_-(B_N, B_s)$, then the real magnetization, M , is zero as expected, whereas the pseudomagnetization is different than zero; indeed, $M_{se}^0 := \lim_{B_N \rightarrow 0} M_{se} = 2 \lim_{B_N \rightarrow 0} \tilde{\mu}_+^{(0)}(B_N, B_s)$, that is

$$M_{se}^0 = \frac{\hbar\tilde{\omega}_{c0}\rho}{2\tilde{B}_0} \mathfrak{M}_0 \left(\frac{B_s}{\tilde{B}_0}, \Delta_R, 1 \right) \quad (81)$$

From this equation, we observe that the pseudo-magnetization emerges as a consequence of the corrugation of the sheet of graphene; in particular, it represents the variation of mechanical energy used by redistributing the charge carriers with pseudospin $\bar{\eta} = \pm 1$. Note that the behavior of the pseudo magnetization versus \tilde{B}_0/B_s , (81), is shown in Fig. 8 b).

Furthermore, if one still considers a non-zero small value of the real magnetic field B_N , one can easily show that

$$M_{se} \approx M_{se}^0 + \left[\left(\frac{\partial M}{\partial B_s} \right) \Big|_{B_N=0} \right] B_N, \quad (82)$$

where the second term indicates that real magnetic fields contribute to the resulting pseudo-magnetization, affecting the form in which the graphene can be deformed due to the charge redistribution by the magnetization.

VIII. CONCLUDING REMARKS

In this paper, we have investigated the magnetization and magnetic susceptibility of strongly curved graphene with and without magnetic fields, employing a continuous effective Dirac equation and a complementary tight-binding study. The results reveal that the magnetization and magnetic susceptibility exhibit discontinuities, following a period of $1/B$, indicative of the Haas van Alphen effect, with a dependence on the sign of the curvature. A nondivergent diamagnetic behavior is observable for low-intensity magnetic fields for both positive and negative curvature cases ($R < 0$ and $R > 0$).

Furthermore, a mechanical effect is also introduced due to the electronic contribution of graphene that gives rise to a pseudo-dHvA effect; this effect is related to oscillating (electronic) forces that oppose the deformations. These forces are divergent in flat graphene, indicating that graphene (without substrate) achieves mechanical equilibrium by corrugations as suggested in other works [115–117]. This implies that in free-standing graphene, the local susceptibility does not diverge. Nevertheless, when strain is applied, or encapsulation is employed, traces of such a divergent susceptibility become experimentally observable as corrugations are eliminated [73]. In the strong curvature regime, the electronic forces opposing deformation are smaller for negatively curved surfaces.

It is worth noting that our model captures the essential physics for low-energy states in relation to a tight-binding model. This is why, in very recent works [118], efforts have been made to construct low-energy operators containing powers of the Dirac operator based on TB models. This approach aims to incorporate accurate information about high-energy states and, as established in our previous works [36, 48], to account for the shift of Dirac cones resulting from strain and the effect of opposite curvatures. Regarding this last point, if we assume the validity of our model as a first approximation, interference and resonance-type effects should be observed.

This is because the sign of curvature appears coupled in the same way as valley indices.

Finally, we conclude by suggesting that the proposed Haas van Alphen effect can be measured in experiments by combining an external magnetic field with induced curvature in a controlled manner. Several strategies exist to do this [36, 48]. One possibility is to use graphene with a nanoscale ripple under an external magnetic field, similar to the device that experimentally measures the valley-dependent Landau levels [94]. Perhaps the most similar experiment to produce the pseudomagnetic field proposed here is the application of a local indentation by an atomic force microscope. Applying a controlled force at the tip of the microscope allows us to obtain a field akin to the one seen in Fig. 1. Another option is to use nanopillars on a suitable dielectric substrate. Therefore, we predict that the applied force needed to keep a specific curvature fixed will show oscillations if the magnetic field changes. All these results and proposals underscore the burgeoning field of *curvatronics* as an area of abundant opportunities.

ACKNOWLEDGMENTS

PCV acknowledges the financial support of SNI-CONAHCyT. AJEC and GGN thanks the CONAHCyT fellowship (No. CVU 1007044) and the Universidad Nacional Autónoma de México (UNAM) for providing financial support (UNAM DGAPA PAPIIT IN101924 and CONAHCyT project 1564464). The authors acknowledge and express gratitude to Thomas Stegmann, and Ramón Carrillo-Bastos for enlightening discussions on the effects of curvature and Carlos Ernesto López Natarén from Secretaria Técnica de Cómputo y Telecomunicaciones for his valuable support to implement high-performance numerical calculations.

Appendix A: Geometric properties of a curved surface with polar symmetry

This Appendix considers a surface with a smooth deformation that preserves polar symmetry embedded in a three-dimensional space described in cylindrical coordinates. The surface is defined by a function $z(r)$. The differential line element for this surface is

$$dl^2 = dr^2 + r^2 d\theta^2 + dz^2 = (1 + \alpha f(r)) dr^2 + r^2 d\theta^2, \quad (A1)$$

where

$$dz^2 = \left(\frac{\partial z(r)}{\partial r} \right)^2 dr^2 \equiv \alpha f(r) dr^2. \quad (A2)$$

Therefore, the spatial part of the metric tensor is

$$g_{ij} = \begin{pmatrix} 1 + \alpha f(r) & 0 \\ 0 & r^2 \end{pmatrix}, \quad (A3)$$

the symbol Γ_{ij}^k gives the affine connection for the above metric, where the non-zero and non-equivalent terms are

$$\begin{aligned} \Gamma_{rr}^r &= \frac{\alpha \partial_r f(r)}{2(1 + \alpha f(r))}, \\ \Gamma_{\theta\theta}^r &= -\frac{r}{1 + \alpha f(r)}, \\ \Gamma_{r\theta}^\theta &= \frac{1}{r}. \end{aligned} \quad (\text{A4})$$

On the other hand, since dreibeins satisfy $g_{\alpha\beta} = e_\alpha^A e_\beta^B \eta_{AB}$, we make the following choice of e_α^A ,

$$\begin{aligned} e_r^1 &= (1 + \alpha f(r))^{1/2} \cos(\theta), \\ e_\theta^1 &= -r \sin(\theta), \\ e_r^2 &= (1 + \alpha f(r))^{1/2} \sin(\theta), \\ e_\theta^2 &= r \cos(\theta). \end{aligned} \quad (\text{A5})$$

Due to this, the non-zero spin connection coefficients ω_μ^{AB} , given by $\omega_\mu^{AB} = e_\nu^A (\partial_\nu + \Gamma_{\mu\lambda}^\nu) e^{B\lambda}$, are

$$\omega_\theta^{12} = 1 - (1 + \alpha f(r))^{-1/2}, \quad (\text{A6})$$

and the spin connection is

$$\Omega_r = 0, \quad \Omega_\theta = \frac{1 - (1 + \alpha f(r))^{-1/2}}{2} \gamma^1 \gamma^2. \quad (\text{A7})$$

Finally, from the definition of the covariant Riemann tensor,

$$R_{\alpha\nu\beta}^\mu = \partial_\nu \Gamma_{\alpha\beta}^\mu - \partial_\beta \Gamma_{\alpha\nu}^\mu + \Gamma_{\alpha\beta}^\sigma \Gamma_{\sigma\nu}^\mu - \Gamma_{\alpha\nu}^\sigma \Gamma_{\sigma\beta}^\mu, \quad (\text{A8})$$

we obtain the Ricci's curvature tensor $R_{\sigma\mu} = R_{\sigma\mu\lambda}^\lambda$

$$\begin{aligned} R_{rr} &= \frac{\alpha \partial_r f(r)}{2r(1 + \alpha f(r))}, \\ R_{\theta\theta} &= \frac{\alpha r \partial_r f(r)}{2(1 + \alpha f(r))^2}. \end{aligned} \quad (\text{A9})$$

Therefore, the scalar curvature $R = g^{\sigma\mu} R_{\sigma\mu}$ is

$$R = \frac{\alpha \partial_r f(r)}{r(1 + \alpha f(r))^2}. \quad (\text{A10})$$

In the case of a specific example given by a Gaussian deformation defined by the function

$$z(r) = z_0 e^{-r^2/(2\varpi^2)}, \quad (\text{A11})$$

where z_0 is the maximum height of the bump and ϖ is the standard deviation around the origin of coordinates. Thus, we obtain that $\alpha f(r)$ and the scalar curvature R are

$$\begin{aligned} \alpha f(r) &= (z_0/\varpi^2)^2 r^2 \exp(-r^2/\varpi^2), \\ R &= \frac{2(z_0/\varpi^2)^2 (1 - (r^2/\varpi^2))}{(1 + (z_0/\varpi^2)^2 r^2 \exp(-r^2/\varpi^2))^2} e^{-r^2/\varpi^2}, \end{aligned} \quad (\text{A12})$$

in this case $\alpha \equiv (z_0/\varpi^2)^2$ controls the type of regime we are in, so $\alpha \ll 1$ and $\alpha \gg 1$ indicate the weak and strong curvature regime, respectively.

Appendix B: The Schrödinger-Lichnerowicz formula

This section will prove the Schrödinger-Lichnerowicz formula. The starting point is the Euclidean Dirac operator $\not{D}_\xi = \underline{\gamma}_\xi^j(x) \nabla_j^\xi$ where $\nabla_j^\xi := (\nabla_j^\xi - iqA_j/\hbar)$ and ∇_j^ξ is the covariant derivative acting on spinors. Now, let us square the operator \not{D}_ξ ,

$$\not{D}_\xi^2 = \left[\frac{1}{2} \{ \underline{\gamma}_\xi^i, \underline{\gamma}_\xi^j \} + \frac{1}{2} [\underline{\gamma}_\xi^i, \underline{\gamma}_\xi^j] \right] \nabla_i^\xi \nabla_j^\xi. \quad (\text{B1})$$

Now, we use the Clifford algebra $\{ \underline{\gamma}_\xi^i, \underline{\gamma}_\xi^j \} = 2g^{ij}$ and the antisymmetric property of the commutator of γ 's to obtain

$$\not{D}_\xi^2 = g^{ij} \nabla_i \nabla_j + \frac{1}{2} \underline{\gamma}_\xi^i \underline{\gamma}_\xi^j [\nabla_i, \nabla_j]. \quad (\text{B2})$$

Next, we apply this operator on a spinor ψ and use the explicit expression of the covariant derivative $\nabla_j^\xi := (\nabla_j^\xi - iqA_j/\hbar)$, just in the second term. Then, one has the second term

$$\begin{aligned} \frac{1}{2} \underline{\gamma}_\xi^i \underline{\gamma}_\xi^j [\nabla_i^\xi, \nabla_j^\xi] &= \frac{1}{2} \underline{\gamma}_\xi^i \underline{\gamma}_\xi^j \left\{ [\nabla_i^\xi, \nabla_j^\xi] - i \frac{q}{\hbar} [\nabla_i^\xi, A_j] \right. \\ &\quad \left. - i \frac{q}{\hbar} [A_i, \nabla_j^\xi] - \frac{q^2}{\hbar^2} [A_i, A_j] \right\}, \end{aligned} \quad (\text{B3})$$

the last term is zero since the gauge field A_i is abelian. The terms in the middle can be simplified as follows $[\nabla_i^\xi, A_j] \psi = (\partial_i A_j) \psi$. Thus, the last equation can be written as

$$\frac{1}{2} \underline{\gamma}_\xi^i \underline{\gamma}_\xi^j [\nabla_i^\xi, \nabla_j^\xi] = \frac{1}{2} \underline{\gamma}_\xi^i \underline{\gamma}_\xi^j \left\{ [\nabla_i^\xi, \nabla_j^\xi] - i \frac{q}{\hbar} (\partial_i A_j - \partial_j A_i) \right\}, \quad (\text{B4})$$

Let us consider $\underline{\gamma}_\xi^i = e_a^i \gamma_\xi^a$, $A_a = e_a^i A_i$, and $\nabla_a^\xi = e_a^i \partial_i$ the covariant derivative acting on vector fields. Therefore, this last expression is,

$$\frac{1}{2} \underline{\gamma}_\xi^i \underline{\gamma}_\xi^j [\nabla_i^\xi, \nabla_j^\xi] = \frac{1}{2} \underline{\gamma}_\xi^i \underline{\gamma}_\xi^j [\nabla_i^\xi, \nabla_j^\xi] - \frac{iq}{2\hbar} \gamma_\xi^a \gamma_\xi^b F_{ab}, \quad (\text{B5})$$

where $F_{ab} = \nabla_a^\xi A_b - \nabla_b^\xi A_a$ is the covariant magnetic strength tensor. The last term in the equation involves the Dirac matrices γ 's (without the underline). Now, we use the following identities

$$[\nabla_i^\xi, \nabla_j^\xi] \psi = \frac{1}{4} R_{ijkl} \underline{\gamma}_\xi^k \underline{\gamma}_\xi^l \psi, \quad (\text{B6})$$

$$\underline{\gamma}_\xi^i \underline{\gamma}_\xi^j \underline{\gamma}_\xi^k \underline{\gamma}_\xi^l R_{ijkl} = -2R, \quad (\text{B7})$$

where R_{ijkl} is the Riemann tensor and R is the Ricci scalar curvature. The above identities can be proven using the $SO(2)$ algebra

$$\frac{1}{4} [\phi_{ab}, \phi_{cd}] = \delta_{ac} \phi_{db} - g_{ad} \phi_{cb} - \delta_{bc} \phi_{da} + \delta_{bd} \phi_{ca}, \quad (\text{B8})$$

where ϕ_{ab} is a 2nd order tensor in $SO(2)$. Also, it is important to use the following expression of the Riemann tensor in terms of the 2-form $\omega_j^a{}_b$

$$R_{ij}{}^{ab} = \partial_i \omega_j^{ab} - \partial_j \omega_i^{ab} + \omega_i^a{}_e \omega_j^{eb} - \omega_j^a{}_e \omega_i^{eb}. \quad (\text{B9})$$

Using these identities, it is not difficult to prove that

$$\mathcal{D}_\xi^2 = g^{ij} \nabla_i^\xi \nabla_j^\xi - \frac{1}{4} R - \frac{iq}{4\hbar} [\gamma_\xi^a, \gamma_\xi^b] F_{ab}. \quad (\text{B10})$$

Using the explicit representation of the γ 's matrices $\gamma_\xi^1 \gamma_\xi^0 = \sigma^1$ and $\gamma_\xi^2 \gamma_\xi^0 = \xi \sigma^2$, we can show that $[\gamma^a, \gamma^b] = 2i\xi \epsilon^{ab} \sigma_3$. Thus, the Schrödinger-Lichnerowicz formula is given by

$$\mathcal{D}_\xi^2 = g^{ij} \nabla_i^\xi \nabla_j^\xi - \frac{1}{4} R + \xi \frac{q}{2\hbar} \sigma_3 \epsilon_{ij} F^{ij}. \quad (\text{B11})$$

Appendix C: Commutation relations

In this section, we will use commutation relations to determine the eigenvalues in two scenarios: a) Weak curvature and b) Strong curvature.

1. Weak curvature regime.

For this, we introduce the operators \hat{v}_i and π_i , given by

$$\begin{aligned} \hat{v}_i &= y_i + \frac{1}{eB_N} \epsilon_{ij} \pi_j, \\ \pi_i &= p_i + \frac{e}{2} B_N \epsilon_{ij} y_j, \end{aligned} \quad (\text{C1})$$

that satisfies the following commutation relations

$$\begin{aligned} [\pi_i, \pi_j] &= i\hbar e B_N \epsilon_{ij}, \\ [\hat{v}_i, \pi_j] &= 0, \\ [\hat{v}_i, \hat{v}_j] &= -\frac{i\hbar}{eB_N} \epsilon_{ij}. \end{aligned} \quad (\text{C2})$$

From (C1) and the definition of angular momentum operator \hat{L} , we obtain that

$$-\hat{L} = \delta^{ij} \left(\frac{1}{2eB_N} \pi_i \pi_j - \frac{eB_N}{2} \hat{v}_i \hat{v}_j \right), \quad (\text{C3})$$

due to the algebraic structure, \hat{L} satisfies that

$$[\hat{L}, \delta^{ij} \pi_i \pi_j] = 0. \quad (\text{C4})$$

Therefore, it is possible to simultaneously diagonalize \hat{L} and π^2 ; for this purpose, we introduce creation operators

$\hat{a}^\dagger, \hat{b}^\dagger$ and annihilation operators \hat{a}, \hat{b}

$$\begin{aligned} \hat{a} &= \sqrt{\frac{1}{2\hbar e B_N}} (\pi_1 + i\pi_2), \\ \hat{a}^\dagger &= \sqrt{\frac{1}{2\hbar e B_N}} (\pi_1 - i\pi_2), \\ \hat{b} &= \sqrt{\frac{eB_N}{2\hbar}} (\hat{v}_1 - i\hat{v}_2), \\ \hat{b}^\dagger &= \sqrt{\frac{eB_N}{2\hbar}} (\hat{v}_1 + i\hat{v}_2), \end{aligned} \quad (\text{C5})$$

that satisfies the following relations

$$\begin{aligned} [\hat{a}, \hat{a}^\dagger] &= 1, \\ [\hat{b}, \hat{b}^\dagger] &= 1, \\ [\hat{a}, \hat{b}] &= 0, \\ [\hat{a}^\dagger, \hat{b}^\dagger] &= 0, \\ [\hat{b}^\dagger, \hat{a}] &= 0, \\ [\hat{a}^\dagger, \hat{b}] &= 0. \end{aligned} \quad (\text{C6})$$

Then, from Eqs. (C1) and (C4), we rewrite the operators π_i and \hat{v}_i , given by

$$\begin{aligned} \pi_1 &= \sqrt{\frac{\hbar e B_N}{2}} (\hat{a} + \hat{a}^\dagger), \\ \pi_2 &= i\sqrt{\frac{\hbar e B_N}{2}} (\hat{a}^\dagger - \hat{a}), \\ \hat{v}_1 &= \sqrt{\frac{\hbar}{2eB_N}} (b + b^\dagger), \\ \hat{v}_2 &= i\sqrt{\frac{\hbar}{2eB_N}} (b - b^\dagger), \end{aligned} \quad (\text{C7})$$

so that the angular momentum operator and the hamiltonian (18) are expressed as

$$\begin{aligned} -\hat{L} &= \hbar (a^\dagger a - b^\dagger b), \\ \tilde{\mathcal{H}}_\xi^2 &= \begin{pmatrix} 2\hbar v_F^2 e B_N (\hat{a}^\dagger \hat{a} + 1/2) & 0 \\ 0 & 2\hbar v_F^2 e B_N (\hat{a}^\dagger \hat{a} + 1/2) \end{pmatrix} \\ &+ \xi \left(e\hbar B_N v_F^2 + \hbar^2 v_F^2 \frac{R}{4} (\hat{b}^\dagger \hat{b} - \hat{a}^\dagger \hat{a}) \right) \sigma_3 \\ &+ \hbar^2 v_F^2 \frac{R}{6} \left((\hat{b}^\dagger \hat{b} - \hat{a}^\dagger \hat{a})^2 + \frac{1}{2} \right) \mathbb{1}. \end{aligned} \quad (\text{C8})$$

The resulting quantum states are quantum harmonic oscillator states like $|n, l\rangle$ with radial quantum number n and angular momenta l that satisfies,

$$\begin{aligned} \hat{a} |n, l\rangle &= \sqrt{n} |n-1, l\rangle, \\ \hat{a}^\dagger |n, l\rangle &= \sqrt{n+1} |n+1, l\rangle, \\ \hat{b} |n, l\rangle &= \sqrt{l} |n, l-1\rangle, \\ \hat{b}^\dagger |n, l\rangle &= \sqrt{l+1} |n, l+1\rangle. \end{aligned} \quad (\text{C9})$$

Therefore, the square root of the eigenvalues of Hamiltonian (C8) are

$$E_{n,m,\tau,\xi,\pm} = \pm \hbar \omega_c \sqrt{n + \frac{1}{2} + \xi \tau \frac{1 + \lambda m}{2} + \frac{\lambda}{3} \left(m^2 + \frac{1}{2} \right)}, \quad (\text{C10})$$

where $\hbar \omega_c = \sqrt{2e\hbar v_F^2 B_N}$, $m = l - n$, $\tau = \pm 1$ is the eigenvalue of σ_3 and represent a pseudo-spin index, $\lambda = \text{sign}(R)B_s/B_N$ with $B_s = \hbar|R|/4e$ is the pseudomagnetic field, $n \in \mathbb{N}$ and $m = -m_{max}, \dots, m_{max}$. As detailed elsewhere [40], $m_{max} = e(B_N + B_s)S/2\pi\hbar$.

2. Strong curvature regime.

In a similar form as in Sec. C1, we introduce the operator $\hat{\Upsilon}_i^{(\tau_R)}$ and $\Pi_i^{(\tau_R)}$, given by

$$\begin{aligned} \hat{\Upsilon}_i^{(\tau_R)} &= y_i + \frac{1}{eB_T^{(\tau_R)}} \epsilon_{ij} \Pi_j^{(\tau_R)}, \\ \Pi_i^{(\tau_R)} &= p_i + \frac{e}{2} B_T^{(\tau_R)} \epsilon_{ij} y^j, \end{aligned} \quad (\text{C11})$$

where we defined the factor $\tau_R \equiv \tau \xi \text{sign}(R) = \pm 1$ and $B_T^{(\tau_R)} = B_N + \tau_R B_s$. These operators satisfy the following commutation relations,

$$\begin{aligned} [\Pi_i^{(\tau_R)}, \Pi_j^{(\tau_R)}] &= i\hbar e B_T^{(\tau_R)} \epsilon_{ij}, \\ [\hat{\Upsilon}_i^{(\tau_R)}, \Pi_j^{(\tau_R)}] &= 0, \\ [\hat{\Upsilon}_i^{(\tau_R)}, \hat{\Upsilon}_j^{(\tau_R)}] &= -\frac{i\hbar}{eB_T^{(\tau_R)}} \epsilon_{ij}. \end{aligned} \quad (\text{C12})$$

From (C11) and the definition of angular momentum operator \hat{L} , we obtain that

$$-\tau_R \hat{L} = \delta^{ij} \left(\frac{1}{2e|B_T^{(\tau_R)}|} \Pi_i^{(\tau_R)} \Pi_j^{(\tau_R)} - \frac{e|B_T^{(\tau_R)}|}{2} \hat{\Upsilon}_i^{(\tau_R)} \hat{\Upsilon}_j^{(\tau_R)} \right), \quad (\text{C13})$$

due to the algebraic structure, \hat{L} satisfies that

$$[\hat{L}, \delta^{ij} \Pi_i^{(\tau_R)} \Pi_j^{(\tau_R)}] = 0. \quad (\text{C14})$$

Therefore, it is possible to simultaneously diagonalize \hat{L} and $\mathbf{\Pi}^2$; for this purpose, we introduce creation operators $\hat{a}_{\tau_R}^\dagger, \hat{b}_{\tau_R}^\dagger$ and annihilation operators $\hat{a}_{\tau_R}, \hat{b}_{\tau_R}$

$$\begin{aligned} \hat{a}_{\tau_R} &= \sqrt{\frac{1}{2\hbar e|B_T^{(\tau_R)}|}} \left(\Pi_1^{(\tau_R)} + i\tau_R \Pi_2^{(\tau_R)} \right), \\ \hat{a}_{\tau_R}^\dagger &= \sqrt{\frac{1}{2\hbar e|B_T^{(\tau_R)}|}} \left(\Pi_1^{(\tau_R)} - i\tau_R \Pi_2^{(\tau_R)} \right), \\ \hat{b}_{\tau_R} &= \sqrt{\frac{e|B_T^{(\tau_R)}|}{2\hbar}} \left(\hat{\Upsilon}_1^{(\tau_R)} - i\tau_R \hat{\Upsilon}_2^{(\tau_R)} \right), \\ \hat{b}_{\tau_R}^\dagger &= \sqrt{\frac{e|B_T^{(\tau_R)}|}{2\hbar}} \left(\hat{\Upsilon}_1^{(\tau_R)} + i\tau_R \hat{\Upsilon}_2^{(\tau_R)} \right), \end{aligned} \quad (\text{C15})$$

that satisfies the following relations

$$\begin{aligned} [\hat{a}_{\tau_R}, \hat{a}_{\tau_R}^\dagger] &= 1, \\ [\hat{b}_{\tau_R}, \hat{b}_{\tau_R}^\dagger] &= 1, \\ [\hat{a}_{\tau_R}, \hat{b}_{\tau_R}] &= 0, \\ [\hat{a}_{\tau_R}^\dagger, \hat{b}_{\tau_R}^\dagger] &= 0, \\ [\hat{b}_{\tau_R}^\dagger, \hat{a}_{\tau_R}] &= 0, \\ [\hat{a}_{\tau_R}^\dagger, \hat{b}_{\tau_R}] &= 0. \end{aligned} \quad (\text{C16})$$

Then, from Eqs. (C11) and (C14), we rewrite the operators $\Pi_i^{(\tau_R)}$ and $\hat{\Upsilon}_i^{(\tau_R)}$, given by

$$\begin{aligned} \Pi_1^{(\tau_R)} &= \sqrt{\frac{\hbar e|B_T^{(\tau_R)}|}{2}} (\hat{a}_{\tau_R} + \hat{a}_{\tau_R}^\dagger), \\ \Pi_2^{(\tau_R)} &= i\tau_R \sqrt{\frac{\hbar e|B_T^{(\tau_R)}|}{2}} (\hat{a}_{\tau_R}^\dagger - \hat{a}_{\tau_R}), \\ \hat{\Upsilon}_1^{(\tau_R)} &= \sqrt{\frac{\hbar}{2e|B_T^{(\tau_R)}|}} (b_{\tau_R} + b_{\tau_R}^\dagger), \\ \hat{\Upsilon}_2^{(\tau_R)} &= i\tau_R \sqrt{\frac{\hbar}{2e|B_T^{(\tau_R)}|}} (b_{\tau_R} - b_{\tau_R}^\dagger), \end{aligned} \quad (\text{C17})$$

so that the angular momentum operator and the hamiltonian (24) are expressed as

$$\begin{aligned} -\tau_R \hat{L} &= \hbar (a_{\tau_R}^\dagger a_{\tau_R} - b_{\tau_R}^\dagger b_{\tau_R}), \\ \tilde{\mathcal{H}}_\xi^2 &= 2\hbar e v_F^2 \left\{ \text{sign}(R) \frac{B_s}{3} \left(\hat{L}^2 + \frac{1}{2} \right) \mathbb{1} \right. \\ &\quad \left. + \frac{1}{2} \begin{pmatrix} \xi B_N & 0 \\ 0 & -\xi B_N \end{pmatrix} \right. \\ &\quad \left. + \begin{pmatrix} |B_T^{(\xi R)}| (\hat{n}_{\xi R} + \frac{1}{2}) & 0 \\ 0 & |B_T^{(-\xi R)}| (\hat{n}_{-\xi R} + \frac{1}{2}) \end{pmatrix} \right\}, \end{aligned} \quad (\text{C18})$$

with $\hat{n}_{\xi R} = \hat{a}_{\xi R}^\dagger \hat{a}_{\xi R}$, and we have introduced the term ξ_R defined by $\xi_R \equiv \text{sign}(R)\xi$. The resulting quantum states are quantum harmonic oscillator states like $|n, l\rangle$ that satisfies

$$\begin{aligned} \hat{a}_{\tau_R} |n, l\rangle &= \sqrt{n} |n-1, l\rangle, \\ \hat{a}_{\tau_R}^\dagger |n, l\rangle &= \sqrt{n+1} |n+1, l\rangle, \\ \hat{b}_{\tau_R} |n, l\rangle &= \sqrt{l} |n, l-1\rangle, \\ \hat{b}_{\tau_R}^\dagger |n, l\rangle &= \sqrt{l+1} |n, l+1\rangle. \end{aligned} \quad (\text{C19})$$

Therefore, the square root of the eigenvalues of Hamiltonian (C18) are

$$E_{n,m,\tau,\xi,\pm} = \pm \hbar \omega_{c,\tau_R} \sqrt{n_{\tau_R} + \frac{1}{2} + \frac{\lambda_{\tau_R}}{3} \left(m_{\tau_R}^2 + \frac{1}{2} \right) + \xi \tau \Theta_{\tau_R}}, \quad (\text{C20})$$

where $\hbar\omega_{c,\tau_R} = \sqrt{2e\hbar v_F^2 |B_T^{(\tau_R)}|}$, $m_{\tau_R} = l_{\tau_R} - n_{\tau_R}$, $\tau = \pm 1$ is the eigenvalue of σ_3 and represent a pseudo-spin index, $\lambda_{\tau_R} = \text{sign}(R)B_s/|B_T^{(\tau_R)}|$, $\Theta_{\tau_R} = B_N/2|B_T^{(\tau_R)}|$ with $B_s = \hbar|R|/4e$ is the pseudomagnetic field, $n \in \mathbb{N}$ and $m_\tau = -m_{max,\tau}, \dots, m_{max,\tau}$. As follows from Ref. [40], $m_{max,\tau} = e|B_T^{(\tau_R)}|S/2\pi\hbar$.

We should note that the treatment for the case $B_N = 0$ has been done previously [40], such that the eigenvalues have a degeneration in the sublattice pseudo-spin and valley index, τ and ξ , i.e.,

$$E_{n,m,\tau,\xi,\pm} = \pm \hbar\omega_c \sqrt{n + \frac{1}{2} + \frac{\text{sign}(R)}{3} \left(m^2 + \frac{1}{2}\right)}, \quad (\text{C21})$$

where $\hbar\omega_c = \sqrt{2e\hbar v_F^2 B_s}$

Appendix D: General functions for free energy, magnetization, and magnetic susceptibility

Let us start with the generic adimensional free-energy

$$\mathfrak{F}_0(\lambda, \Delta, \bar{f}) = \lambda^{3/2} \sum_{n=-\infty}^{\lfloor \frac{1}{\lambda} - \bar{f} \rfloor} \text{sign}(n) \sqrt{|n| + \Delta}. \quad (\text{D1})$$

This series can be written in terms of the Riemann zeta function $\zeta_R(p)$, and Hurwitz zeta function, $\zeta_H(p, q)$, defined as

$$\zeta_R(p) \equiv \sum_{n=1}^{\infty} \frac{1}{n^p}; \quad \zeta_H(p, q) \equiv \sum_{n=0}^{\infty} \frac{1}{(n+q)^p}. \quad (\text{D2})$$

Using the sum property of the Hurwitz function, one can simplify the free energy Eq. (D1),

$$\mathfrak{F}_0(\lambda, \Delta, \bar{f}) = -\lambda^{3/2} \zeta_H \left(-\frac{1}{2}, \left[\frac{1}{\lambda} - \bar{f} \right] + 1 + \Delta \right). \quad (\text{D3})$$

To calculate the magnetization, we need to differentiate the previous equation with respect to B_s or B_N . By using the following identities [7],

$$\begin{aligned} \partial \zeta_H(p, q) / \partial q &= -p \zeta_H(p+1, q), \\ \partial [x] / \partial x &= \sum_{n \in \mathbb{Z}} \delta(x-n), \end{aligned} \quad (\text{D4})$$

and because Δ depends on B_N and B_s , we can separate the adimensional magnetization per unit area into three additive terms. The first two terms are,

$$\begin{aligned} \mathfrak{M}_0(\lambda, \Delta, \bar{f}) &= \left\{ \frac{3\lambda^{1/2}}{2} \zeta_H \left(-\frac{1}{2}, \left[\frac{1}{\lambda} - \bar{f} \right] + 1 + \Delta \right) \right. \\ &\quad \left. - \frac{1}{2} \lambda^{-1/2} \zeta_H \left(\frac{1}{2}, \left[\frac{1}{\lambda} - \bar{f} \right] + 1 + \Delta \right) \sum_{n \in \mathbb{Z}} \delta \left(n - \frac{1}{\lambda} + \bar{f} \right) \right\}, \\ \mathfrak{M}_1(\lambda, \Delta, \bar{f}) &= \lambda^{-1/2} \zeta_H \left(\frac{1}{2}, \left[\frac{1}{\lambda} - \bar{f} \right] + 1 + \Delta \right). \end{aligned} \quad (\text{D5})$$

The third term is proportional to the derivative $\partial \bar{f} / \partial B$ where $B = B_s$ or $B = B_N$ depending on the required case. However, this term is multiplied by a sum of Dirac delta functions. It only produces a marginal contribution at each magnetization jump produced when an LL is filled. Therefore, we will not consider this correction here, although we numerically confirm that it is marginal to the result. Finally, the magnetic susceptibility, obtained by differentiating the previous two magnetizations with respect to the fields, is,

$$\begin{aligned} \mathfrak{S}_0(\lambda, \Delta, \bar{f}) &= \left\{ \frac{3}{4} \lambda^{-1/2} \zeta_H \left(-\frac{1}{2}, \left[\frac{1}{\lambda} - \bar{f} \right] + 1 + \Delta \right) \right. \\ &\quad \left. - \frac{1}{2} \lambda^{-3/2} \zeta_H \left(\frac{1}{2}, \left[\frac{1}{\lambda} - \bar{f} \right] + 1 + \Delta \right) \right. \\ &\quad \times \sum_{n \in \mathbb{Z}} \delta \left(n - \frac{1}{\lambda} + \bar{f} \right) \\ &\quad \left. - \frac{1}{4} \lambda^{-5/2} \zeta_H \left(\frac{3}{2}, \left[\frac{1}{\lambda} - \bar{f} \right] + 1 + \Delta \right) \right. \\ &\quad \times \sum_{n,m \in \mathbb{Z}} \delta \left(m - \frac{1}{\lambda} + \bar{f} \right) \delta \left(n - \frac{1}{\lambda} + \bar{f} \right) \\ &\quad \left. - \frac{1}{2} \lambda^{-5/2} \zeta_H \left(\frac{1}{2}, \left[\frac{1}{\lambda} - \bar{f} \right] + 1 + \Delta \right) \right. \\ &\quad \left. \times \sum_{m \in \mathbb{Z}} \delta'(x) \Big|_{x=m-\frac{1}{\lambda}+\bar{f}} \right\}, \quad \bar{n} \geq 1, \end{aligned} \quad (\text{D6})$$

$$\begin{aligned} \mathfrak{S}_1(\mathbf{b}_1, \lambda, \Delta, \bar{f}) &= \frac{\mathbf{b}_1}{12} \\ &\quad \times \left\{ 2\lambda^{-3/2} \zeta_H \left(\frac{1}{2}, \left[\frac{1}{\lambda} - \bar{f} \right] + 1 + \Delta \right) \right. \\ &\quad \left. - \frac{\mathbf{b}_1}{3} \lambda^{-5/2} \zeta_H \left(\frac{3}{2}, \left[\frac{1}{\lambda} - \bar{f} \right] + 1 + \Delta \right) \right. \\ &\quad \left. + 2\lambda^{-5/2} \zeta_H \left(\frac{3}{2}, \left[\frac{1}{\lambda} - \bar{f} \right] + 1 + \Delta \right) \right. \\ &\quad \left. \times \sum_{n \in \mathbb{Z}} \delta \left(n - \frac{1}{\lambda} + \bar{f} \right) \right\} \end{aligned} \quad (\text{D7})$$

In the previous equations, we again neglected terms proportional to $\partial \bar{f} / \partial B$. Notice that all the previous equations are mathematically valid whenever

$$\left[\frac{1}{\lambda} - \bar{f} \right] + \Delta + 1 \geq 0.$$

In our problem, such a condition is always satisfied as the Fermi level is always bigger than zero.

In Fig. 9, we show the thermodynamical properties oscillating behavior for different curvatures and for the possible values of pseudo-spin coupling index $\bar{\eta} = \pm 1$. If we compare with the total part seen in Fig. 7, we can understand how the interference effect appears due to the different contributions.

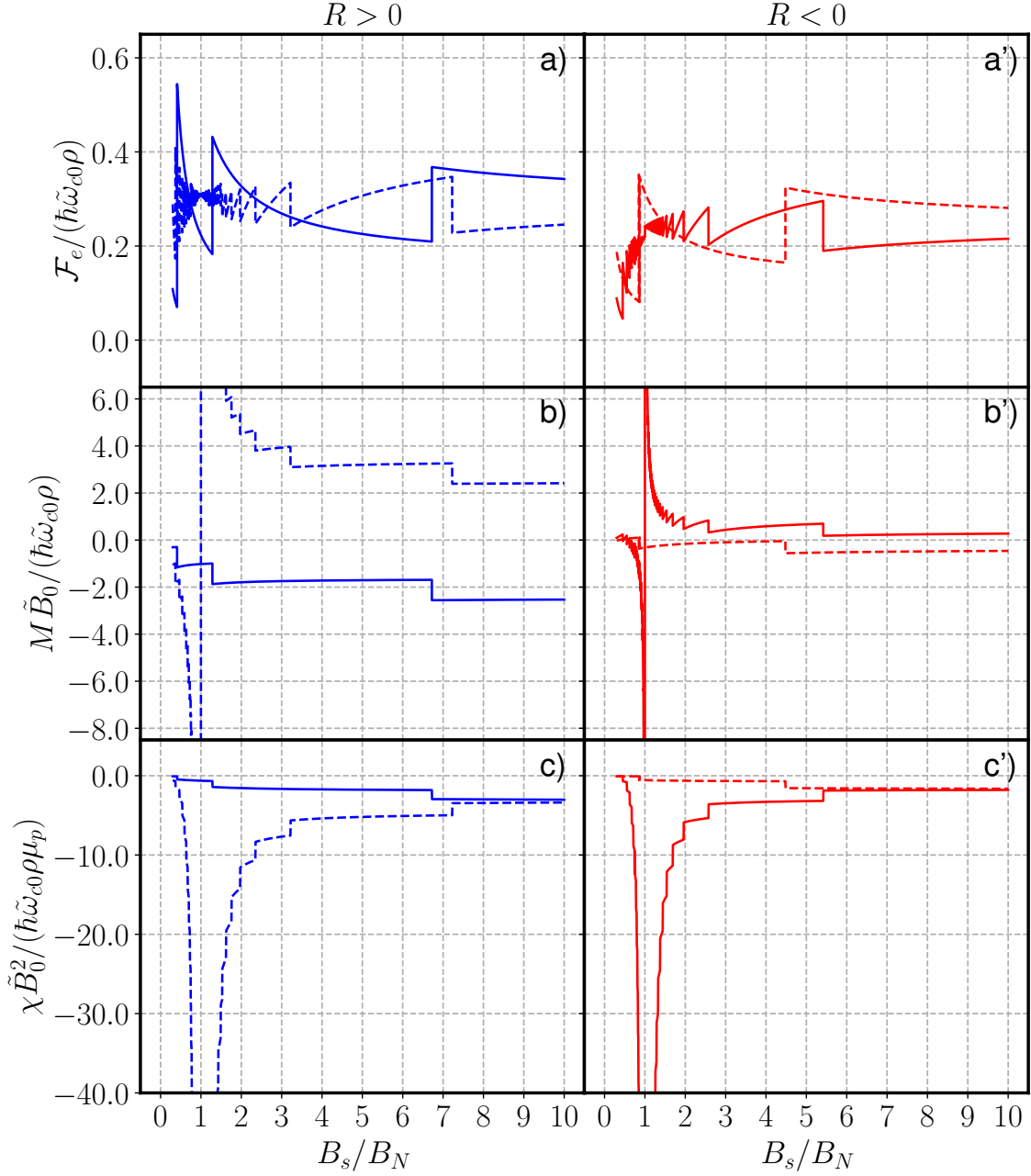


FIG. 9. Electronic contribution in the, a) Helmholtz free energy (Eq. (61)), b) magnetization (Eq. (67)), and c), magnetic susceptibility (Eq. (69)) as a function of B_s/B_N for two different curvatures $R > 0$ (blue lines) and $R < 0$ (red lines) separated into their respective two different pseudo-spin coupling index contributions, $\bar{\eta} = 1$ (solid lines) and $\bar{\eta} = -1$ (dashed lines), respectively. The interference effect seen in Fig. 7 is due to the different pseudo-spin coupling contributions presented here. Taken into account that $\rho \sim 2 \times 10^{18} m^{-2}$ [114], $B_s \sim 300$ T [104], the total field used for making these plots is $\tilde{B}_0 = \hbar\pi\rho/4e \sim 1033.47$ T.

- [1] De W J Haas and P M Van Alphen. The dependence of the susceptibility of diamagnetic metals upon the field. *Proc. Acad. Sci. Amst.*, 1106–1118, 1930.
 [2] Ning Ma, Zaur Z. Alisultanov, and M.S. Reis. Exter-

nal mechanisms for valley polarisation and its effect on the magnetisation of graphene: strain and electric field. *Journal of Magnetism and Magnetic Materials*, 482:178–185, July 2019.

- [3] Shengli Zhang, Ning Ma, and Erhu Zhang. The modulation of the de Haas–van Alphen effect in graphene by electric field. *Journal of Physics: Condensed Matter*, 22(11):115302, March 2010.
- [4] M. A. Wilde, M. P. Schwarz, Ch. Heyn, D. Heitmann, D. Grundler, D. Reuter, and A. D. Wieck. Experimental evidence of the ideal de Haas–van Alphen effect in a two-dimensional system. *Physical Review B*, 73(12):125325, March 2006.
- [5] Israel D Vagner. Thermodynamics of two-dimensional electrons on Landau levels. *HIT Journal of Science and Engineering A*, 3(1):102–152, mar 2006.
- [6] V. B. Pluzhnikov, I. V. Svechkarev, A. V. Dukhnenko, A. V. Levchenko, V. B. Filippov, and A. Chopnik. de Haas–van Alphen effect in the diborides ScB₂, ZrB₂, and HfB₂. *Low Temperature Physics*, 33(4):350–354, April 2007.
- [7] F. R. Pratama, M. Shoufie Ukhtary, and Riichiro Saito. Magnetizations and de Haas–van Alphen oscillations in massive Dirac fermions. *Physical Review B*, 103(24):245408, June 2021.
- [8] D. Shoenberg. The de haas–van alphen effect in copper. *Nature*, 183(4655):171–171, Jan 1959.
- [9] D. Shoenberg. *Magnetic Oscillations in Metals*. Cambridge Monographs on Physics. Cambridge University Press, 1984.
- [10] Igor A. Luk’yanchuk. De Haas–van Alphen effect in 2D systems: application to mono- and bilayer graphene. *Low Temperature Physics*, 37(1):45–48, January 2011.
- [11] S. V. Kryuchkov, E. I. Kukhar’, and P. V. Nazarov. Influence of high-frequency electromagnetic radiation on the de Haas–van Alphen effect in graphene. *Bulletin of the Russian Academy of Sciences: Physics*, 80(2):190–193, February 2016.
- [12] Biwu Dong, Wanjun Sun, Daqing Liu, and Ning Ma. The mechanical strain induced anomalous de Haas–van Alphen effect on graphene. *Physica B: Condensed Matter*, 577:411824, Jan 2020.
- [13] T. Champel and V. P. Mineev. de Haas–van Alphen effect in two- and quasi-two-dimensional metals and superconductors. *Philosophical Magazine B*, 81(1):55–74, Jan 2001.
- [14] Juuso Manninen, Antti Laitinen, Francesco Massel, and Pertti Hakonen. Mechanical detection of the de haas–van alphen effect in graphene. *Nano Letters*, 22(24):9869–9875, Dec 2022.
- [15] D. Shoenberg and William Lawrence Bragg. The de haas–van alphen effect. *Philosophical Transactions of the Royal Society of London. Series A, Mathematical and Physical Sciences*, 245(891):1–57, 1952.
- [16] D. Shoenberg. Chapter viii the de haas–van alphen effect, 1957.
- [17] D. Shoenberg. The de haas–van alphen effect in copper, silver and gold. *The Philosophical Magazine: A Journal of Theoretical Experimental and Applied Physics*, 5(50):105–110, 1960.
- [18] T. Holstein, R. E. Norton, and P. Pincus. de haas–van alphen effect and the specific heat of an electron gas. *Phys. Rev. B*, 8:2649–2656, Sep 1973.
- [19] D. Shoenberg. Evidence from the de haas–van alphen effect. *Physik der kondensierten Materie*, 9(1):1–14, Mar 1969.
- [20] D Shoenberg. Theory of the de haas–van alphen effect. *Journal of Physics F: Metal Physics*, 18(1):49, jan 1988.
- [21] Zhen-Guo Fu, Zhi-Gang Wang, Shu-Shen Li, and Ping Zhang. Magnetic quantum oscillations in a monolayer graphene under a perpendicular magnetic field. *Chinese Physics B*, 20(5):058103, May 2011.
- [22] S. G. Sharapov, V. P. Gusynin, and H. Beck. Magnetic oscillations in planar systems with the dirac-like spectrum of quasiparticle excitations. *Physical Review B*, 69(7):075104, feb 2004.
- [23] Sergey Slizovskiy and Joseph J. Betouras. Nonlinear magnetization of graphene. *Physical Review B*, 86(12):125440, September 2012.
- [24] Zhilin Li, Lianlian Chen, Sheng Meng, Liwei Guo, Jiao Huang, Yu Liu, Wenjun Wang, and Xiaolong Chen. Field and temperature dependence of intrinsic diamagnetism in graphene: Theory and experiment. *Phys. Rev. B*, 91:094429, Mar 2015.
- [25] L. Landau. Diamagnetismus der metalle. *Zeitschrift für Physik*, 64(9):629–637, Sep 1930.
- [26] L. Onsager. Interpretation of the de haas–van alphen effect. *The London, Edinburgh, and Dublin Philosophical Magazine and Journal of Science*, 43(344):1006–1008, 1952.
- [27] R. Peierls. Zur theorie des diamagnetismus von leitungselektronen. ii starke magnetfelder. *Zeitschrift für Physik*, 81(3):186–194, Mar 1933.
- [28] Yong Liu, Tao Ma, Lin Zhou, Warren E. Straszheim, Farhan Islam, Brandt A. Jensen, Wei Tian, Thomas Heitmann, R. A. Rosenberg, J. M. Wilde, Bing Li, Andreas Kreyssig, Alan I. Goldman, B. G. Ueland, Robert J. McQueeney, and David Vaknin. Crystal growth, microstructure, and physical properties of SrMnSb₂. *Physical Review B*, 99(5):054435, February 2019.
- [29] M. A. Wilde, D. Reuter, Ch. Heyn, A. D. Wieck, and D. Grundler. Inversion-asymmetry-induced spin splitting observed in the quantum oscillatory magnetization of a two-dimensional electron system. *Phys. Rev. B*, 79:125330, Mar 2009.
- [30] Zhigang Wang, Wei Zhang, and Ping Zhang. Magnetization in two-dimensional electron gas in a perpendicular magnetic field: The roles of edge states and spin-orbit coupling. *Phys. Rev. B*, 79:235327, Jun 2009.
- [31] I. Meinel, T. Hengstmann, D. Grundler, D. Heitmann, W. Wegscheider, and M. Bichler. Magnetization of the fractional quantum hall states. *Phys. Rev. Lett.*, 82:819–822, Jan 1999.
- [32] K. S. Novoselov, A. K. Geim, S. V. Morozov, D. Jiang, Y. Zhang, S. V. Dubonos, I. V. Grigorieva, and A. A. Firsov. Electric field effect in atomically thin carbon films. *Science*, 306(5696):666–669, 2004.
- [33] P. R. Wallace. The band theory of graphite. *Phys. Rev.*, 71:622–634, May 1947.
- [34] M. Oliva-Leyva and Gerardo G. Naumis. Understanding electron behavior in strained graphene as a reciprocal space distortion. *Phys. Rev. B*, 88:085430, Aug 2013.
- [35] M. Oliva-Leyva and Gerardo G. Naumis. Generalizing the fermi velocity of strained graphene from uniform to nonuniform strain. *Physics Letters A*, 379(40):2645–2651, 2015.
- [36] Gerardo G Naumis, Salvador Barraza-Lopez, Maurice Oliva-Leyva, and Humberto Terrones. Electronic and optical properties of strained graphene and other strained 2d materials: a review. *Reports on Progress in Physics*, 80(9):096501, aug 2017.
- [37] A. Cortijo and M. A. H. Vozmediano. A cosmological model for corrugated graphene sheets. *The European*

- Physical Journal Special Topics, 148(1):83–89, 2007.
- [38] A. H. Castro Neto, F. Guinea, N. M. R. Peres, K. S. Novoselov, and A. K. Geim. The electronic properties of graphene. *Rev. Mod. Phys.*, 81:109–162, Jan 2009.
- [39] Fernando de Juan, Mauricio Sturla, and María A. H. Vozmediano. Space dependent fermi velocity in strained graphene. *Phys. Rev. Lett.*, 108:227205, May 2012.
- [40] Pavel Castro-Villarreal and R. Ruiz-Sánchez. Pseudomagnetic field in curved graphene. *Phys. Rev. B*, 95:125432, Mar 2017.
- [41] Abdiel E. Champo, Pedro Roman-Taboada, and Gerardo G. Naumis. Landauer-büttiker conductivity for spatially-dependent uniaxial strained armchair-terminated graphene nanoribbons. *Physica E: Low-dimensional Systems and Nanostructures*, 102:123–131, 2018.
- [42] Abdiel Espinosa-Champo and Gerardo G. Naumis. Multifractal wavefunctions of charge carriers in graphene with folded deformations, ripples, or uniaxial flexural modes: Analogies to the quantum hall effect under random pseudomagnetic fields. *Journal of Vacuum Science & Technology B*, 39(6):062202, 2021.
- [43] Si-Yu Li, Ying Su, Ya-Ning Ren, and Lin He. Valley polarization and inversion in strained graphene via pseudolandau levels, valley splitting of real landau levels, and confined states. *Phys. Rev. Lett.*, 124:106802, Mar 2020.
- [44] Bitan Roy. Odd integer quantum hall effect in graphene. *Phys. Rev. B*, 84:035458, Jul 2011.
- [45] Bitan Roy, Zi-Xiang Hu, and Kun Yang. Theory of unconventional quantum hall effect in strained graphene. *Phys. Rev. B*, 87:121408, Mar 2013.
- [46] Pablo A. Morales and Patrick Copinger. Curvature-induced pseudogauge fields from time-dependent geometries in graphene. *Phys. Rev. B*, 107:075432, Feb 2023.
- [47] Glenn Wagner, Fernando de Juan, and Dung X. Nguyen. Landau levels in curved space realized in strained graphene. *SciPost Phys. Core*, 5:029, 2022.
- [48] Gerardo G Naumis, Saúl A Herrera, Shiva P Poudel, Hiro Nakamura, and Salvador Barraza-Lopez. Mechanical, electronic, optical, piezoelectric and ferroic properties of strained graphene and other strained monolayers and multilayers: an update. *Reports on Progress in Physics*, 87(1):016502, nov 2023.
- [49] Long-Jing Yin, Ke-Ke Bai, Wen-Xiao Wang, Si-Yu Li, Yu Zhang, and Lin He. Landau quantization of dirac fermions in graphene and its multilayers. *Frontiers of Physics*, 12(4):127208, 2017.
- [50] D. Faria, C. León, L. R. F. Lima, A. Latgé, and N. Sandler. Valley polarization braiding in strained graphene. *Phys. Rev. B*, 101:081410, Feb 2020.
- [51] Dawei Zhai and Nancy Sandler. Local versus extended deformed graphene geometries for valley filtering. *Phys. Rev. B*, 98:165437, Oct 2018.
- [52] G. M. M. Wakker, Rakesh P. Tiwari, and M. Blaauboer. Localization and circulating currents in curved graphene devices. *Phys. Rev. B*, 84:195427, Nov 2011.
- [53] Haibiao Zhou, Nadav Auerbach, Matan Uzan, Yaozhang Zhou, Nasrin Banu, Weifeng Zhi, Martin E. Huber, Kenji Watanabe, Takashi Taniguchi, Yuri Myasoedov, Binghai Yan, and Eli Zeldov. Imaging quantum oscillations and millitesla pseudomagnetic fields in graphene. *Nature*, 624(7991):275–281, 2023.
- [54] C.-C. Hsu, M. L. Teague, J.-Q. Wang, and N.-C. Yeh. Nanoscale strain engineering of giant pseudo-magnetic fields, valley polarization, and topological channels in graphene. *Science Advances*, 6(19):eaat9488, 2020.
- [55] Paola Gentile, Mario Cuoco, Oleksii M. Volkov, Zujian Ying, Ivan J. Vera-Marun, Denys Makarov, and Carmine Ortix. Electronic materials with nanoscale curved geometries. *Nature Electronics*, 5(9):551–563, 2022.
- [56] Yi-Wen Liu and Lin He. Recent progresses on graphene-based artificial nanostructures: a perspective from scanning tunneling microscopy. *Quantum Frontiers*, 2(1):2, 2023.
- [57] Dawei Zhai and Nancy Sandler. Electron dynamics in strained graphene. *Modern Physics Letters B*, 33(28):1930001, 2019.
- [58] Anita Bhagat and Kieran Mullen. Pseudo-magnetic quantum Hall effect in oscillating graphene. *Solid State Communications*, 287:31–34, Jan 2019.
- [59] Víctor A. González-Domínguez, Juan A. Reyes-Nava, and Pavel Castro-Villarreal. Klein tunneling on hour surfaces with n topological defects. *Phys. Rev. B*, 108:195421, Nov 2023.
- [60] Pedro Roman-Taboada and Gerardo G. Naumis. Topological flat bands in time-periodically driven uniaxial strained graphene nanoribbons. *Phys. Rev. B*, 95:115440, Mar 2017.
- [61] Pedro Roman-Taboada and Gerardo G. Naumis. Topological edge states on time-periodically strained armchair graphene nanoribbons. *Phys. Rev. B*, 96:155435, Oct 2017.
- [62] Pedro Roman-Taboada and Gerardo G Naumis. Topological phase-diagram of time-periodically rippled zigzag graphene nanoribbons. *Journal of Physics Communications*, 1(5):055023, dec 2017.
- [63] Jinhai Mao, Slaviša P. Milovanović, Miša Andelković, Xinyuan Lai, Yang Cao, Kenji Watanabe, Takashi Taniguchi, Lucian Covaci, Francois M. Peeters, Andre K. Geim, Yuhang Jiang, and Eva Y. Andrei. Evidence of flat bands and correlated states in buckled graphene superlattices. *Nature*, 584(7820):215–220, 2020.
- [64] Antonio L R Manesco and Jose L Lado. Correlation-induced valley topology in buckled graphene superlattices. *2D Materials*, 8(3):035057, jun 2021.
- [65] A L R Manesco, J L Lado, E V S Ribeiro, G Weber, and D Rodrigues Jr. Correlations in the elastic landau level of spontaneously buckled graphene. *2D Materials*, 8(1):015011, oct 2020.
- [66] S. P. Milovanović, M. Andelković, L. Covaci, and F. M. Peeters. Band flattening in buckled monolayer graphene. *Phys. Rev. B*, 102:245427, Dec 2020.
- [67] Md Tareq Mahmud, Dawei Zhai, and Nancy Sandler. Topological flat bands in strained graphene: Substrate engineering and optical control. *Nano Letters*, 23(16):7725–7732, 2023. PMID: 37578461.
- [68] R. Carrillo-Bastos, D. Faria, A. Latgé, F. Mireles, and N. Sandler. Gaussian deformations in graphene ribbons: Flowers and confinement. *Phys. Rev. B*, 90:041411, Jul 2014.
- [69] R. Carrillo-Bastos, C. León, D. Faria, A. Latgé, E. Y. Andrei, and N. Sandler. Strained fold-assisted transport in graphene systems. *Phys. Rev. B*, 94:125422, Sep 2016.
- [70] L. N. Monteiro, C. A. S. Almeida, and J. E. G. Silva. Dirac fermions on wires confined to the graphene möbius strip. *Phys. Rev. B*, 108:115436, Sep 2023.
- [71] Marco Cariglia, Roberto Giambò, and Andrea Perali. Curvature-tuned electronic properties of bilayer

- graphene in an effective four-dimensional spacetime. *Phys. Rev. B*, 95:245426, Jun 2017.
- [72] Thomas Stegmann and Nikodem Szpak. Current splitting and valley polarization in elastically deformed graphene. *2D Materials*, 6(1):015024, dec 2018.
- [73] J. Vallejo Bustamante, N. J. Wu, C. Fermon, M. Pannetier-Lecoecur, T. Wakamura, K. Watanabe, T. Taniguchi, T. Pellegrin, A. Bernard, S. Daddi-nounou, V. Bouchiat, S. Guéron, M. Ferrier, G. Montambaux, and H. Bouchiat. Detection of graphene's divergent orbital diamagnetism at the dirac point. *Science*, 374(6573):1399–1402, 2021.
- [74] Antonio Gallerati. Graphene, dirac equation and analogue gravity. *Physica Scripta*, 97(6):064005, may 2022.
- [75] Tommaso Morresi, Daniele Binosi, Stefano Simonucci, Riccardo Piergallini, Stephan Roche, Nicola M Pugno, and Taioli Simone. Exploring event horizons and hawking radiation through deformed graphene membranes. *2D Materials*, 7(4):041006, sep 2020.
- [76] M.D. Pollock. On the Dirac equation in curved spacetime. *Acta Phys. Polon. B*, 41:1827–1846, 2010.
- [77] T. Frankel. *The Geometry of Physics: An Introduction*. Cambridge University Press, 2004.
- [78] Dai-Nam Le, Anh-Luan Phan, Van-Hoang Le, and Pinaki Roy. Spherical fullerene molecules under the influence of electric and magnetic fields. *Physica E: Low-dimensional Systems and Nanostructures*, 107:60–66, March 2019.
- [79] O Boada, A Celi, J I Latorre, and M Lewenstein. Dirac equation for cold atoms in artificial curved spacetimes. *New Journal of Physics*, 13(3):035002, 2011.
- [80] A Pnueli. Spinors and scalars on Riemann surfaces. *Journal of Physics A: Mathematical and General*, 27(4):1345–1352, February 1994.
- [81] Dai-Nam Le, Van-Hoang Le, and Pinaki Roy. Electric field and curvature effects on relativistic Landau levels on a pseudosphere. *Journal of Physics: Condensed Matter*, 31(30):305301, July 2019.
- [82] Mehmet Ali Olpak. Dirac equation on a curved (2+1)-dimensional hypersurface. *Modern Physics Letters A*, 27(03):1250016, 2012.
- [83] Mark Burgess and Bjo/rn Jensen. Fermions near two-dimensional surfaces. *Physical Review A*, 48(3):1861–1868, September 1993.
- [84] F.T. Brandt and J.A. Sánchez-Monroy. Dirac equation on a curved surface. *Physics Letters A*, 380(38):3036–3043, September 2016.
- [85] Dai-Nam Le, Anh-Luan Phan, Van-Hoang Le, and Pinaki Roy. Relativistic Coulomb problem in curved spaces. *EPL (Europhysics Letters)*, 127(1):10005, August 2019.
- [86] Giulio Ferrari and Giampaolo Cuoghi. Schrödinger Equation for a Particle on a Curved Surface in an Electric and Magnetic Field. *Physical Review Letters*, 100(23):230403, June 2008.
- [87] M. Nakahara. *Geometry, Topology and Physics*. CRC Press, 2018.
- [88] Richard Kerner, Gerardo G. Naumis, and Wilfrido A. Gómez-Arias. Bending and flexural phonon scattering: Generalized dirac equation for an electron moving in curved graphene. *Physica B: Condensed Matter*, 407(12):2002–2008, 2012.
- [89] Dean Moldovan and Miša Anđelković and Francois Peeters. pybinding v0.9.5: a Python package for tight-binding calculations, aug 2020. This work was supported by the Flemish Science Foundation (FWO-VI) and the Methusalem Funding of the Flemish Government.
- [90] J. W. McClure. Diamagnetism of graphite. *Phys. Rev.*, 104:666–671, Nov 1956.
- [91] Luther Pfahler Eisenhart. *Riemannian Geometry*. Princeton University Press, 1997.
- [92] David Toms Leonard Parker. *Quantum Field Theory in Curved Spacetime: Quantized Fields and Gravity*. Cambridge Monographs on Mathematical Physics. Cambridge University Press, 1 edition, 2009.
- [93] Uwe Muller, Christian Schubert, and Anton E. M. van de Ven. A closed formula for the riemann normal coordinate expansion. *General Relativity and Gravitation*, 31(11):1759–1768, 1999.
- [94] Si-Yu Li, Ying Su, Ya-Ning Ren, and Lin He. Valley polarization and inversion in strained graphene via pseudo-landau levels, valley splitting of real landau levels, and confined states. *Phys. Rev. Lett.*, 124:106802, Mar 2020.
- [95] M.I. Katsnelson. *Graphene: Carbon in Two Dimensions*. Cambridge University Press, 2012.
- [96] Daniel Cangemi and Gerald Dunne. Temperature expansions for magnetic systems. *Annals of Physics*, 249(2):582–602, 1996.
- [97] M. Reis. *Fundamentals of Magnetism*. Elsevier Science, 2013.
- [98] P.D. Beale. *Statistical Mechanics*. Elsevier Science, 2011.
- [99] M. Sepioni, R. R. Nair, S. Rablen, J. Narayanan, F. Tuna, R. Winpenny, A. K. Geim, and I. V. Grigorieva. Limits on intrinsic magnetism in graphene. *Phys. Rev. Lett.*, 105:207205, Nov 2010.
- [100] Lianlian Chen, Liwei Guo, Yue Wu, Yuping Jia, Zhilin Li, and Xiaolong Chen. Fabrication of vertically aligned graphene sheets on sic substrates. *RSC Adv.*, 3:13926–13933, 2013.
- [101] P. Xu, Yurong Yang, S. D. Barber, M. L. Ackerman, J. K. Schoelz, D. Qi, Igor A. Kornev, Lifeng Dong, L. Bellaiche, Salvador Barraza-Lopez, and P. M. Thibado. Atomic control of strain in freestanding graphene. *Phys. Rev. B*, 85:121406, Mar 2012.
- [102] P. Xu, J. K. Schoelz, S. D. Barber, M. L. Ackerman, and P. M. Thibado. Broad frequency and amplitude control of vibration in freestanding graphene via scanning tunneling microscopy with calculated dynamic pseudo-magnetic fields. *Journal of Applied Physics*, 112(12):124317, 12 2012.
- [103] C. S. C. Downs, A. Usher, and J. Martin. Towards observation of pseudo-magnetic fields in suspended graphene devices. *Journal of Applied Physics*, 119(19):194305, 05 2016.
- [104] N Levy, S A Burke, K L Meaker, M Panlasigui, A Zettl, F Guinea, A H Castro Neto, and M F Crommie. Strain-induced pseudo-magnetic fields greater than 300 tesla in graphene nanobubbles. *Science*, 329(5991):544–547, Jul 2010.
- [105] L.D. Landau, E.M. Lifshitz, A.M. Kosevich, E.M. Lifshitz, and L.P. Pitaevskii. *Theory of Elasticity: Volume 7. Course of theoretical physics*. Elsevier Science, 1986.
- [106] A.E. Green and W. Zerna. *Theoretical Elasticity*. Dover Books on engineering. Dover Publications, 1992.
- [107] H. Terrones, M. Terrones, and W. K. Hsu. Beyond c60: graphite structures for the future. *Chem. Soc. Rev.*, 24:341–350, 1995.
- [108] H. W. Kroto, J. R. Heath, S. C. O'Brien, R. F. Curl,

- and R. E. Smalley. C60: Buckminsterfullerene. Nature, 318(6042):162–163, 1985.
- [109] Alan Lindsay Mackay, H. Terrones, Patrick William Fowler, Harold Walter Kroto, Alan Lindsay Mackay, Grenville Turner, and D. R. M. Walton. Hypothetical graphite structures with negative gaussian curvature. Philosophical Transactions of the Royal Society of London. Series A: Physical and Engineering Sciences, 343(1667):113–127, 1993.
- [110] Humberto Terrones and Alan L. Mackay. From c60 to negatively curved graphite. Progress in Crystal Growth and Characterization of Materials, 34(1):25–36, 1997.
- [111] Humberto Terrones. Curved graphite and its mathematical transformations. Journal of Mathematical Chemistry, 15(1):143–156, 1994.
- [112] Zhongwei Zhang, Jie Chen, and Baowen Li. Negative gaussian curvature induces significant suppression of thermal conduction in carbon crystals. Nanoscale, 9:14208–14214, 2017.
- [113] Efrem Braun, Yongjin Lee, Seyed Mohamad Moosavi, Senja Barthel, Rocio Mercado, Igor A. Baburin, Davide M. Proserpio, and Berend Smit. Generating carbon schwarzites via zeolite-templating. Proceedings of the National Academy of Sciences, 115(35):E8116–E8124, 2018.
- [114] Juuso Manninen, Antti Laitinen, Francesco Massel, and Pertti Hakonen. Mechanical detection of the de haas–van alphen effect in graphene. Nano Letters, 22(24):9869–9875, 12 2022.
- [115] Jannik C. Meyer, A. K. Geim, M. I. Katsnelson, K. S. Novoselov, T. J. Booth, and S. Roth. The structure of suspended graphene sheets. Nature, 446(7131):60–63, 2007.
- [116] A. Fasolino, J. H. Los, and M. I. Katsnelson. Intrinsic ripples in graphene. Nature Materials, 6(11):858–861, 2007.
- [117] Sebastian Fischetti, Lucas Wallis, and Toby Wiseman. What spatial geometries do (2+1)-dimensional quantum field theory vacua prefer? Phys. Rev. Lett., 120:261601, Jun 2018.
- [118] Matthew M. Roberts and Toby Wiseman. Analog gravity and continuum effective theory of the graphene tight-binding lattice model. Phys. Rev. B, 109:045425, Jan 2024.